

# **Development of a polymer MEMS characterization system**

by

Calin Plesa

A THESIS SUBMITTED IN PARTIAL FULFILLMENT  
OF THE REQUIREMENTS FOR THE DEGREE OF  
BACHELOR OF APPLIED SCIENCE  
in the School  
of  
Engineering Science

Calin Plesa ©2008  
SIMON FRASER UNIVERSITY  
January 9, 2008

All rights reserved. This work may not be  
reproduced in whole or in part, by photocopy  
or other means, without the permission of the author.

# Approval

**Name:** Calin Plesa  
**Degree:** Bachelor of Applied Science  
**Title of Thesis:** Development of a polymer MEMS characterization system

---

Dr. Mehrdad Saif  
Director  
School of Engineering Science, SFU

## Examining Committee:

### Chair, Academic and Technical Supervisor:

---

Dr. Ash Parameswaran  
Professor  
School of Engineering Science, SFU

### Committee Member:

---

Dr. Karen Kavanagh  
Professor  
Department of Physics, SFU

### Committee Member:

---

Mike Sjoerdsma  
Lecturer  
School of Engineering Science, SFU

**Date Approved:** \_\_\_\_\_

# Abstract

This thesis describes the development of a system which quickly characterizes the material properties in a polymer MEMS process. A drop-in test die was created containing a variety of mechanical test structures, which can be placed in wafer layouts as necessary. After the wafer fabrication process, the test die is separated and placed into a holder which can be mechanically actuated in plane. The system sweeps the frequency used to drive the actuator while capturing microscope images. Software analysis of the images is used to determine the resonance frequency of each test structure as well as its physical dimensions. With these data, the Young's modulus of the polymer is determined. This technique was tested on a SU-8 based microfabrication process. The results from different test structures are compared along with the sources of error that affect them.

# Acknowledgements

I would like to thank Dan Sameoto for his help with beam theory, fabrication issues, as well as taking the time to fabricate the test wafers used in this project. Thanks to See-Ho Tsang also for his assistance with LabVIEW and Vision. Special thanks to Dr. Ash Parameswaran for his advice and for providing me the opportunity to work in such a great research environment.

# Table of Contents

<b>Approval .....</b>	<b>ii</b>
<b>Abstract.....</b>	<b>iii</b>
<b>Acknowledgements .....</b>	<b>iv</b>
<b>List of Figures.....</b>	<b>vi</b>
<b>List of Tables .....</b>	<b>vii</b>
<b>1. Introduction.....</b>	<b>1</b>
<b>2. Theory .....</b>	<b>4</b>
<b>3. Testing System Hardware .....</b>	<b>8</b>
3.1. Piezoelectric Actuator .....	9
3.2. Actuator Control .....	11
3.3. Microscope and Image Capture .....	12
<b>4. Test Die .....</b>	<b>13</b>
<b>5. Software .....</b>	<b>15</b>
<b>6. Operational Procedure .....</b>	<b>19</b>
<b>7. Sources of Error .....</b>	<b>22</b>
7.1. Non-Linear Duffing Effect .....	22
7.2. Negative Sidewalls.....	23
7.3. Image Analysis.....	27
7.4. Density .....	31
<b>8. Results .....</b>	<b>32</b>
8.1. Young's Modulus.....	33
8.2. Error due to Operation in Air.....	38
8.3. Sample Degradation.....	39
<b>9. Finite Element Analysis.....</b>	<b>40</b>
<b>Conclusion and Future Work .....</b>	<b>43</b>
<b>References.....</b>	<b>44</b>
<b>Appendix A: imgFIX Source Code.....</b>	<b>46</b>
<b>Appendix B: Ideal Resonance Frequencies .....</b>	<b>50</b>

# List of Figures

Figure 1 - The in-plane motion of a fixed-free beam on the left and a fixed-fixed beam on the right. ....	6
Figure 2 - Finding the Q factor from the frequency response.....	7
Figure 3 - An overview of the hardware setup .....	8
Figure 4 - A 0.5 cm die on the stacked piezoelectric actuator.....	10
Figure 5 - The displacement curve for the stacked actuator. ....	10
Figure 6 - Resistance characteristics for the 4-stack piezoelectric actuator being used. ....	11
Figure 7 - A set of short beam cantilevers of length varying from 200 $\mu\text{m}$ to 1000 $\mu\text{m}$ . ....	14
Figure 8 - Some fixed-fixed beams of length varying from 800 $\mu\text{m}$ to 2000 $\mu\text{m}$ . ....	14
Figure 9 - The full layout of the test die showing the structures and the resulting material properties measured. ....	14
Figure 10 - A screenshot of the frequency sweep control program. ....	16
Figure 11 - A screenshot of the Vision inspection used to determine physical dimensions...	17
Figure 12 - Measuring the amplitude of oscillation using Vision's caliper function. ....	18
Figure 13 - High level overview of the testing procedure. ....	20
Figure 14 - The frequency response of a cantilever operating in the non-linear region, image courtesy of V. Kaajakari, T. Mattila, A. Oja, and H. Seppä [7]. ....	22
Figure 15 - A beam with trapezoidal cross-section. ....	23
Figure 16 - Measuring the negative sidewall using the pop-up structure and NI Vision. ....	24
Figure 17 - The error introduced into the value of Young's modulus calculated as a function of the sidewall angle. ....	25
Figure 18 - The error in calculated Young's modulus due to uncertainty in the value of the negative sidewall angle. ....	26
Figure 19 - The start of the length measurement at the fixed end where beams are attached to the anchor is shown on the left. The end of the measurement at the rounded free ends is shown on the right.....	27
Figure 20 - The error introduced into the calculated value of Young's modulus by an error of several pixels in the length measurement of an 1800 $\mu\text{m}$ Long Beam. ....	28
Figure 21 - The error introduced into the calculated value of Young's modulus by an error of several pixels in the length measurement of a 600 $\mu\text{m}$ Short Beam. ....	28
Figure 22 - The error introduced into the calculated value of Young's modulus by an error of several pixels in the width measurement of an 1800 $\mu\text{m}$ Long Beam. ....	29
Figure 23 - The error introduced into the calculated value of Young's modulus by an error of several pixels in the width measurement of a 600 $\mu\text{m}$ Short Beam. ....	29
Figure 24 – Left: A 15 $\mu\text{m}$ beam as seen with a 25x objective. The edges appear out of focus due to the sidewall. Right: The same beam observed using a 50x objective.....	30
Figure 25 - The maximum in plane projection of the sidewall as a function of the sidewall angle.....	31
Figure 26 - The error of a mismatch between the real density and the value used.....	31
Figure 27 - The layout of the test dies around the wafer, their baking temperature on the left. The dies tested and the dies with defects on the right.....	32

Figure 28 - Distribution of Young's modulus from the all of the structures on the 120°C test dies is shown on the left and just the data from Long Beams on the right. ....	34
Figure 29 - The experimentally observed differences between the behaviour of Poly1 and Poly2 beams within a set of Long Beams and a set of Short Beams. ....	35
Figure 30 - Theoretical predictions of the behaviour of the same test structures presented in Figure 29. ....	35
Figure 31 - A non-linear curve fit using one set of Poly1 Long Beams. ....	37
Figure 32 - Response of three Short Beams of varying length. ....	38
Figure 33 - The normalized response of three beams one week and ten weeks after fabrication. ....	39
Figure 34 - Experimentally observed response of Poly2 Short 15 $\mu\text{m}$ Beam 6, compared with the results of a harmonic analysis for both rectangular and trapezoidal cross sections..	41
Figure 35 - Experimentally observed response of Poly2 Short 15 $\mu\text{m}$ Beam 4, compared with the results of a harmonic analysis. ....	42
Figure 36 - The FEM predicted response for three values of Young's modulus using the rectangular beam model and the observed response. ....	42

## List of Tables

Table 1 - Three common polymers and their Young's modulus. ....	1
Table 2 - A comparison of various testing techniques. ....	2
Table 3 - Boundary conditions for fixed and free beams ends [3]. ....	4
Table 4 - The coefficients for the first three resonance modes. ....	5
Table 5 - A breakdown of the costs associated with this system. ....	8
Table 6 - The scaling parameters at four magnifications for the Moticam 1300 camera. ....	12
Table 7 - The scaling parameters for the BigCatch EM-500M camera. ....	12
Table 8 - An overview of the various test structures found on the test die. ....	13
Table 9 - Negative sidewall data for different dies and test structures. ....	24
Table 10 - Depth of field for different power microscope objectives. ....	30
Table 11 - The values of Young's modulus calculated from the four 120°C test dies. ....	33
Table 12 - A list of values for the Young's modulus of SU-8 found in publications. ....	34
Table 13 - The values of Young's modulus calculated from the two 95°C test dies. ....	36
Table 14 - Curve fits for the four sets of Long Beams. ....	36
Table 15 - The Q factors, damping ratio, and corresponding error for four beams. ....	39
Table 16 - A comparison of the modal frequencies calculated in Ansys and the experimental results. ....	40
Table 17 - The ideal resonance frequencies of the high aspect Short Beams. ....	50
Table 18 - The frequencies of the first two modes for the low aspect ratio Long Beams. ....	50

# 1. Introduction

The work behind this project arises from the need for a quick and cheap system for determining material properties of polymers, including the Young's modulus, tensile stress, stress gradient, and Poisson's ratio. Microscale devices are fabricated using multi-step fabrication processes. Because each wafer fabrication run has slightly different process parameters, a diagnostic test die is needed which can be placed into a wafer layout in order to quickly determine the resulting parameters for each run. Such a system could be used to determine the source of process errors and increase yield. It could also investigate the effects of a variety of environmental factors, such as humidity and temperature on polymer materials, which are largely undocumented. A better understanding of the material properties will also improve device simulations. The diagnostic system outlined in this thesis provides a cost-effective solution to address these issues.

**Table 1 - Three common polymers and their Young's modulus.**

<b>Polymer</b>	<b>Young's Modulus (GPa) [1]</b>
SU-8	2 - 5
Polyimide	2.5
PMMA	1.8 – 3.1

Several polymers which could be tested with this system along with their modulus are shown in Table 1. The properties of these materials can be changed with additives such as metal particles and carbon nanotubes. Relatively little literature exists on the properties of these novel materials. This project was tested with a pure SU-8 photo patternable polymer. Polymers are gaining popularity in the micro-electrical-mechanical-systems (MEMS) field



due to their unique properties, low-costs, biocompatibility, and low processing temperatures. They can be used to fabricate various types of sensors, actuators, and microfluidic components.

Several methods of ascertaining material properties were examined to determine the method best suited for polymer materials. A list of the most popular testing techniques, compared in a previously published paper [2], is shown in Table 2.

**Table 2 - A comparison of various testing techniques.**

Capabilities of microscale testing techniques						Test structures compatible with test techniques				
Test	$E$	$\sigma_y$	$\sigma_f$	$\sigma_r$	$\nabla \sigma_r$	Thin	Thick	Free	Constrained	Integrated
Tension	✓	✓	✓			✓	✓	✓		No
Plate bend			✓				✓	✓		No
Microbeam bend	✓	✓	✓			✓	✓	✓		No
Bulge test	✓			✓		✓		✓		No
M-test	✓			✓		✓		✓		Yes
Wafer curvature				✓		✓	✓		✓	No
Resonance	✓			✓		✓	✓	✓		Yes
Strain gages				✓	✓	✓	✓	✓		Yes

Electrostatic techniques (M-test) were ruled out since the polymers being tested are non-conductive, and adding metal layers would interfere with the measurements. With the exception of the resonance and strain gage techniques, a major downside of the other methods is that they can not be integrated on-chip. Integrated techniques allow active devices on the same wafer as the test structures, whereas non-integrated methods must have a separate test wafer specifically fabricated. Since material properties can vary from run to run

due to slight changes in processing conditions, using an integrated technique has advantages. Many other methods also require a probe to physically test each structure, which is slow and often requires expensive equipment. The resonance test described in this thesis uses an external vibration source which can actuate all of the structures on a die, and potentially an entire wafer, at once. This simultaneous vibration enables parallel testing and reduces the uncertainty in the final results.

Photo patternable polymers are well suited to the resonance technique due to their low stiffness, which allows creating cantilevers with in-plane resonance frequencies less than 25 kHz and allows the use of low cost piezoelectric actuators as the external vibration source. The polymers targeted by this system all have a Young's modulus less than 10 GPa. This method cannot be used with Silicon due to its high stiffness and correspondingly high resonance frequencies. Because of optical measurements, the technique can produce values within minutes and the number of structures tested at once is limited only by the size of the microscope's field of view. Another advantage of this method is the cost required to setup this system. The test setup consists of a CCD camera, voltage amplifier, piezoelectric actuator, and a control computer. With the exception of the piezoelectric actuator and the high-voltage amplifier needed to drive it, most of the hardware required is already available in many labs. The resonance method lends itself as the ideal approach to measuring the material properties of polymers.

## 2. Theory

The behaviour of the structures being tested can be predicted using Euler-Bernoulli beam theory. The motion for a beam with rectangular cross section is governed by the fourth order differential equation [3]

$$\frac{\partial^2 w(x,t)}{\partial t^2} + \frac{EI}{\rho A} \frac{\partial^4 w(x,t)}{\partial x^4} = 0 , \quad (1)$$

where  $I$  is the moment of inertia,  $E$  is Young's modulus,  $\rho$  is the density, and  $A$  is the cross-sectional area of beam. Using separation of variables, the equation is split into spatial and temporal parts. The general solution to the spatial equation is

$$X(x) = a_1 \sin(\beta \cdot x) + a_2 \cos(\beta \cdot x) + a_3 \sinh(\beta \cdot x) + a_4 \cosh(\beta \cdot x) , \quad (2)$$

where

$$\beta^4 = \frac{\rho A \omega^2}{EI} . \quad (3)$$

Applying the boundary conditions shown in Table 3 leads to a system of four equations.

**Table 3 - Boundary conditions for fixed and free beams ends [3] .**

Boundary Conditions for a Free Beam End	Boundary Conditions for a Fixed Beam End
bending moment = $EI \frac{\partial^2 w}{\partial x^2} = 0$	deflection = $w = 0$
shear force = $\frac{\partial}{\partial x} \left[ EI \frac{\partial^2 w}{\partial x^2} \right] = 0$	slope = $\frac{\partial w}{\partial x} = 0$

In the case of a fixed-free beam, setting the determinant of the coefficient matrix to zero leads to the characteristic equation

$$\cos(\beta \cdot L) \cosh(\beta \cdot L) = 1 , \quad (4)$$

where  $L$  is the length of the beam. Each solution of this equation is a coefficient ( $C_n$ ) corresponding to a resonance mode of the beam. The coefficients for the first three modes of resonance are shown in Table 4 for both types of beams used.

**Table 4 - The coefficients for the first three resonance modes.**

Mode	Fixed-Free Coefficient ( $C_n$ )	Fixed-Fixed Coefficient ( $C_n$ )
1	3.52	22.37
2	22.03	61.67
3	61.70	120.9

The moment of inertia for a rectangular beam undergoing in-plane motion is

$$I = \frac{T \cdot W^3}{12} , \quad (5)$$

where  $T$  is the beam's thickness. The in-plane motion of the two types of beams used is shown in Figure 1. The resonance frequency is given by

$$\omega = C_n \sqrt{\frac{k}{m}} = C_n \sqrt{\frac{3EI}{mL^3}} = C_n \sqrt{\frac{E \cdot W^2}{12 \cdot \rho \cdot L^4}} , \quad (6)$$

where  $k$  is the stiffness and  $W$  is the beam's width.

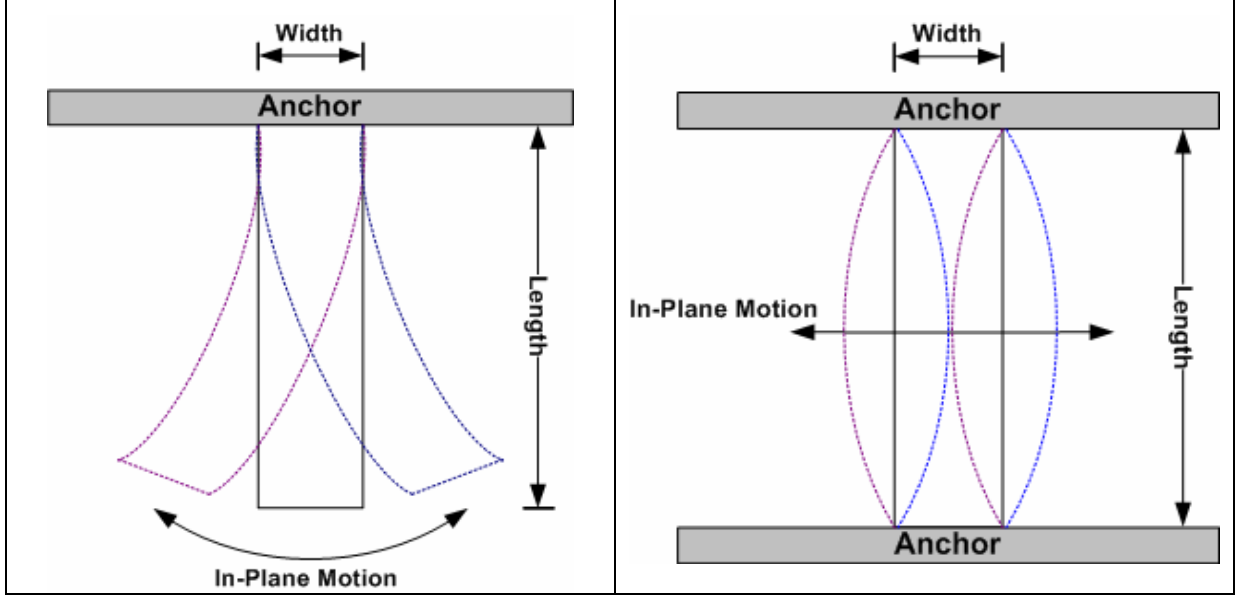


**Figure 1 - The in-plane motion of a fixed-free beam on the left and a fixed-fixed beam on the right.**

In the case of the fixed-fixed beam, the shrinkage caused by the manufacturing process causes a tensile stress in the beam. The tensile stress increases the resonance frequency of the beam by a factor of

$$\omega = \omega_0 \sqrt{1 + B_n \frac{\sigma \cdot L^2}{E \cdot W^2}} , \quad (7)$$

where  $B_n$  is a constant equal to 1.22 and  $\sigma$  is the tensile stress. The tensile stress can thus be calculated using

$$\sigma_r = \frac{\pi^2 E \cdot W^2}{12L^2} \left[ \left( \frac{2\sqrt{12}}{\pi} \frac{f \cdot L^2}{W} \sqrt{\frac{\rho}{E}} \right)^2 - 1 \right] . \quad (8)$$

Actuating the test structures in air as opposed to vacuum will introduce further damping which will lower the resonance frequency by

$$f_d = f_n \sqrt{1 - \zeta^2} , \quad (9)$$

where  $f_d$  is the damped frequency,  $f_n$  is the natural frequency, and  $\zeta$  is the damping ratio.

The damping ratio can be determined by measuring the frequency response, calculating the Q factor, and using the relation

$$Q = \frac{1}{2 \cdot \zeta} . \quad (10)$$

The Q factor is determined by measuring the frequency response of a test structure as shown in Figure 2.

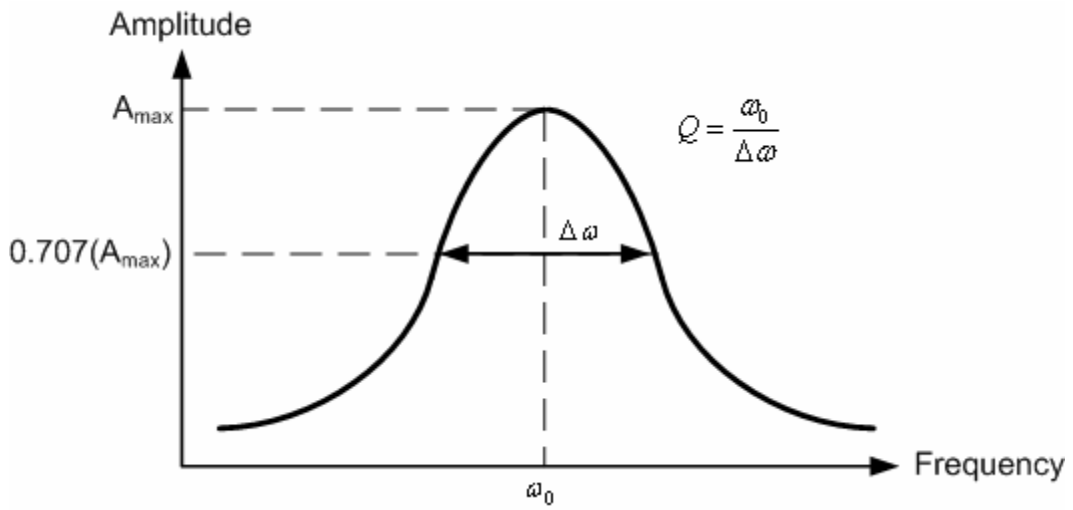


**Figure 2 - Finding the Q factor from the frequency response.**

### 3. Testing System Hardware

Figure 3 shows the basic setup for the testing system. Much of the equipment needed for this setup is common in most MEMS labs. The computer gathers image data from the camera while outputting a control signal to the voltage amplifier.

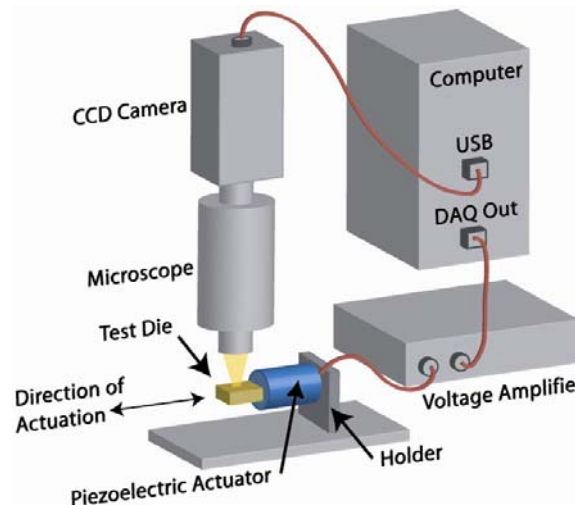


**Figure 3 - An overview of the hardware setup**

One of the advantages points of this system is its low cost of implementation; the estimated cost of implementation is outlined in Table 5.

**Table 5 - A breakdown of the costs associated with this system.**

Hardware	Estimated Cost (\$)
Camera	500
Microscope	7000
Piezoelectric Actuator	500
Amplifier	4000
Function Generator PC Card	2700
<b>Software</b>	
Vision	1800
LabVIEW	3000
<b>TOTAL</b>	<b>19500</b>

### 3.1. Piezoelectric Actuator

The mechanical actuation of the test chip is achieved through the use of a piezoelectric actuator. Selecting a good actuator is a critical aspect of this system's design. The best device will have a large resonance frequency and be capable of producing a large displacement. The displacement of a piezoelectric actuator is given by

$$\Delta L = n \cdot d_{33} \cdot V , \quad (11)$$

where  $n$  is the number of elements in the stack,  $d_{33}$  is the strain parallel to the polarization axis, and  $V$  is the applied voltage. The piezoelectric coefficient ( $d_{33}$ ) depends on the piezoelectric material used. In many cases, the limiting factor in this setup will be the large signal bandwidth of the amplifier used, which is the range of frequencies over which the amplifier can output a waveform with less than 1% distortion. By using a stacked actuator with many elements, the operating voltage can be significantly reduced; smaller voltages open the possibility of using a low-voltage function generator, which can provide a much wider bandwidth.

The displacement characteristics of two different actuators were measured by observing the edge of each piezoelectric element under a microscope's maximum magnification, while a high-voltage square wave was applied. The first actuator was a large rectangular block of Lead Zirconate Titanate (PZT) with silver electrodes on two opposing faces. Its displacement remained below the microscope's optical threshold (137 nm) even with 600 V applied. The second actuator, shown in Figure 4, was a 4 element stacked piezoelectric actuator initially designed for an underwater sonar array. It showed



displacements of 400 nm at 400 V and 540 nm at 500 V. Using Equation 11, the value of  $d_{33}$  was calculated as  $2.6 \times 10^{-10}$  m/V, which indicates that the stacked actuator is also made of Lead Zirconate Titanate (PZT) [4] . This coefficient was used to predict the displacement curve shown in Figure 5. In actuality, the displacement curve has a hysteresis effect proportional to the distance traveled.

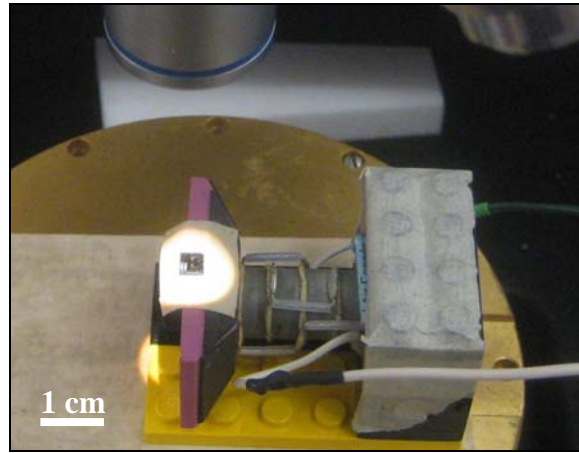


**Figure 4 - A 0.5 cm die on the stacked piezoelectric actuator.**

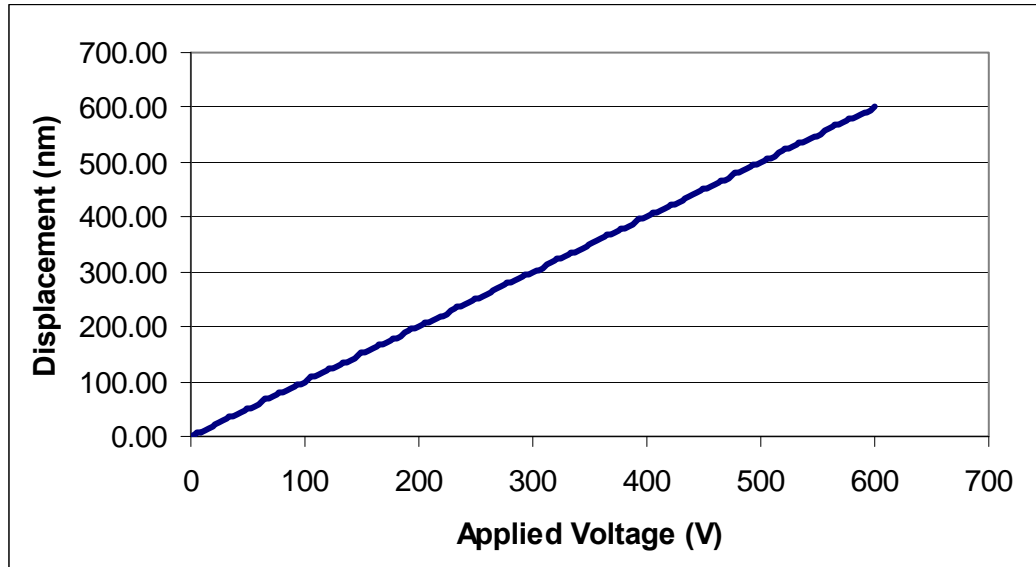


**Figure 5 - The displacement curve for the stacked actuator.**

The response characteristics, shown in Figure 6, were measured by connecting a function generator to one terminal of the actuator and a resistive load to the other. The input and load voltages were recorded while the frequency of the signal was swept. The minimum resistance measured at 25.1 kHz corresponds to the actuator's resonance frequency, the point where the electro-mechanical coupling is greatest.

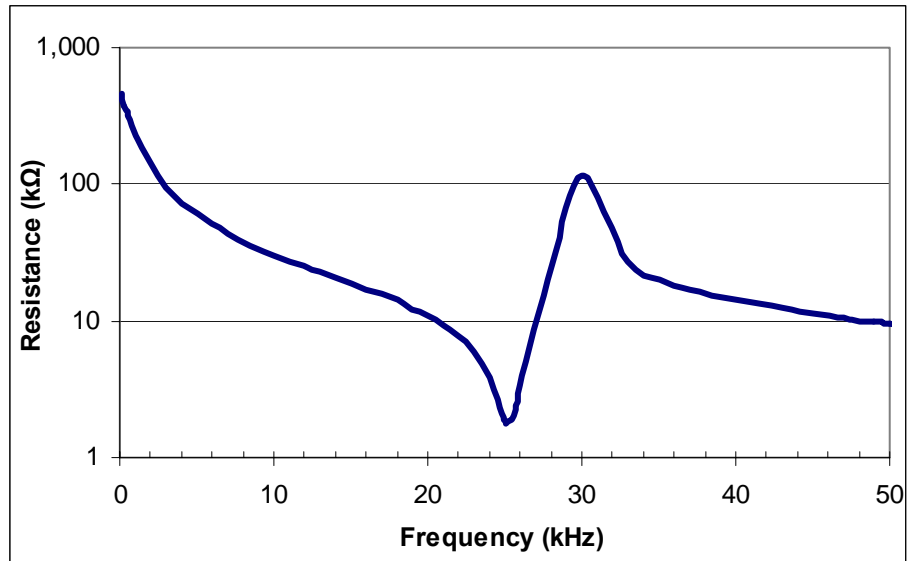


**Figure 6 - Resistance characteristics for the 4-stack piezoelectric actuator being used.**

Future systems will use a shear actuator with a resonance frequency over 200 kHz and a maximum displacement greater than 3  $\mu\text{m}$ . This actuator will provide access to the test structure's higher resonance modes which are beyond the reach of the 25.1 kHz actuator.

### **3.2. Actuator Control**

The piezoelectric actuator is driven by a TREK model PZD700 high voltage amplifier capable of outputting up to 700 V. Its large signal bandwidth has been experimentally

determined to be around 15 kHz. The amplifier is controlled through a signal outputted by a NI PCI-5401 function generator card on the control computer.

### 3.3. Microscope and Image Capture

The microscope used was a Micromanipulator Co. Model 6000 with a Moticam 1300 FireWire camera attached. The camera is capable of capturing 1024 x 768 pixel images at one second intervals. When used in conjunction with the 2.25x microscope objective, the camera has a maximum viewing area of 3.15 x 2.37 mm. Image measurements are converted to actual distance using the scaling parameters shown in Table 6. Due to a 6% difference between the length and width of the pixels on the camera's sensor, different parameters are used for each axis.

**Table 6 - The scaling parameters at four magnifications for the Moticam 1300 camera.**

	<b>Motic Moticam 1300 (1024 x 768)</b>							
<b>Axis</b>	Vertical (768 pixels)				Horizontal (1025 pixels)			
<b>Objective</b>	2.25x		25x		2.25x		25x	
<b>Eyepiece Zoom</b>	Max	Min	Max	Min	Max	Min	Max	Min
<b>Scaling (<math>\mu\text{m}/\text{pixel}</math>)</b>	1.800	3.386	0.159	0.261	1.712	3.173	0.137	0.226

A 5.17 Mega-pixel BigCatch EM-500M USB2.0 eyepiece camera also became available during the course of this project. It can capture 2592 x 1944 pixel images and has a viewing area of 5.04 x 3.78 mm. This camera has a significantly lower refresh rate and is best suited to capturing static images. The scaling parameters used are shown in Table 7.

**Table 7 - The scaling parameters for the BigCatch EM-500M camera.**

	<b>BigCatch EM-500M (2592x1944)</b>			
<b>Objective</b>	2.25x		25x	
<b>Eyepeice Zoom</b>	Max	Min	Max	Min
<b>Scaling (<math>\mu\text{m}/\text{px}</math>)</b>	0.9937	1.9846	0.0871	0.1718

## 4. Test Die

The 1 x 1 cm test die, shown in Figure 9, contains three groups of dynamic structures including low and high aspect ratio fixed-free beams (Figure 7), as well as fixed-fixed beams (Figure 8). It was designed by Dan Sameoto using the L-Edit layout program made by Tanner Research. All of the groups outlined in Table 8, with the exception of the low aspect ratio beams, can fit within the microscope's field of view, which allows all of the test structures within the group to be tested simultaneously. The ideal resonance frequencies for the fixed-free test structures are provided in Appendix B.

**Table 8 - An overview of the various test structures found on the test die.**

Group Name	Design Width (μm)	Lengths (μm)	Beam Type	Number of beams for each layer	Layers (Thickness)	Aspect Ratio
10 μm Short Beams	10	200 to 1000	Fixed-Free	9	Poly 1 (18 μm)	High
					Poly 2 (38 μm)	High
15 μm Short Beams	15	200 to 1000	Fixed-Free	9	Poly 1 (18 μm)	High
					Poly 2 (38 μm)	High
10 μm Fixed Beams	10	800 to 2000	Fixed-Fixed	4	Poly 1 (18 μm)	High
					Poly 2 (38 μm)	High
15 μm Fixed Beams	15	800 to 2000	Fixed-Fixed	4	Poly 1 (18 μm)	High
					Poly 2 (38 μm)	High
Long Beams	75	200 to 3200	Fixed-Free	16	Poly 1 (18 μm)	Low
					Poly 2 (38 μm)	Low

Two static structures, strain gauges and 90° pop-up structures are also used. The Tsang plate pop-up structure, designed by See-Ho Tsang [5] is used for curvature, thickness, and negative sidewall angle measurement. The strain gauge is used to determine the residual stress and its gradient, as outlined in Table 2. The initial test die was fabricated using the custom SU-8 polymer process developed in-house at SFU [6] .

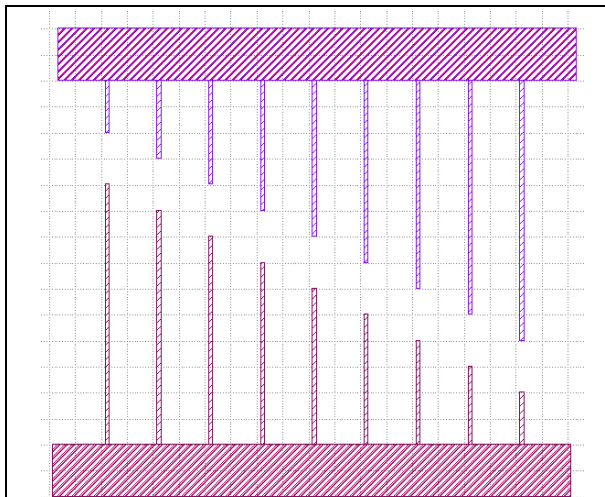


**Figure 7 - A set of short beam cantilevers of length varying from 200  $\mu\text{m}$  to 1000  $\mu\text{m}$ .**

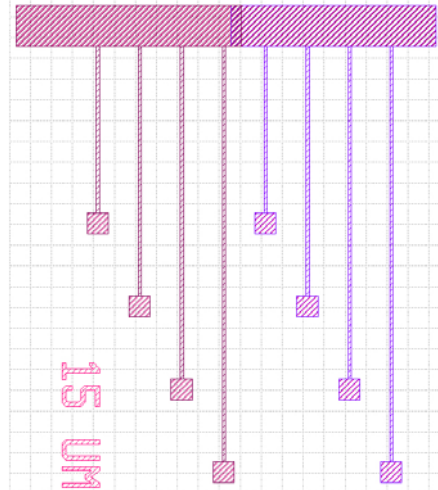


**Figure 8 - Some fixed-fixed beams of length varying from 800  $\mu\text{m}$  to 2000  $\mu\text{m}$ .**

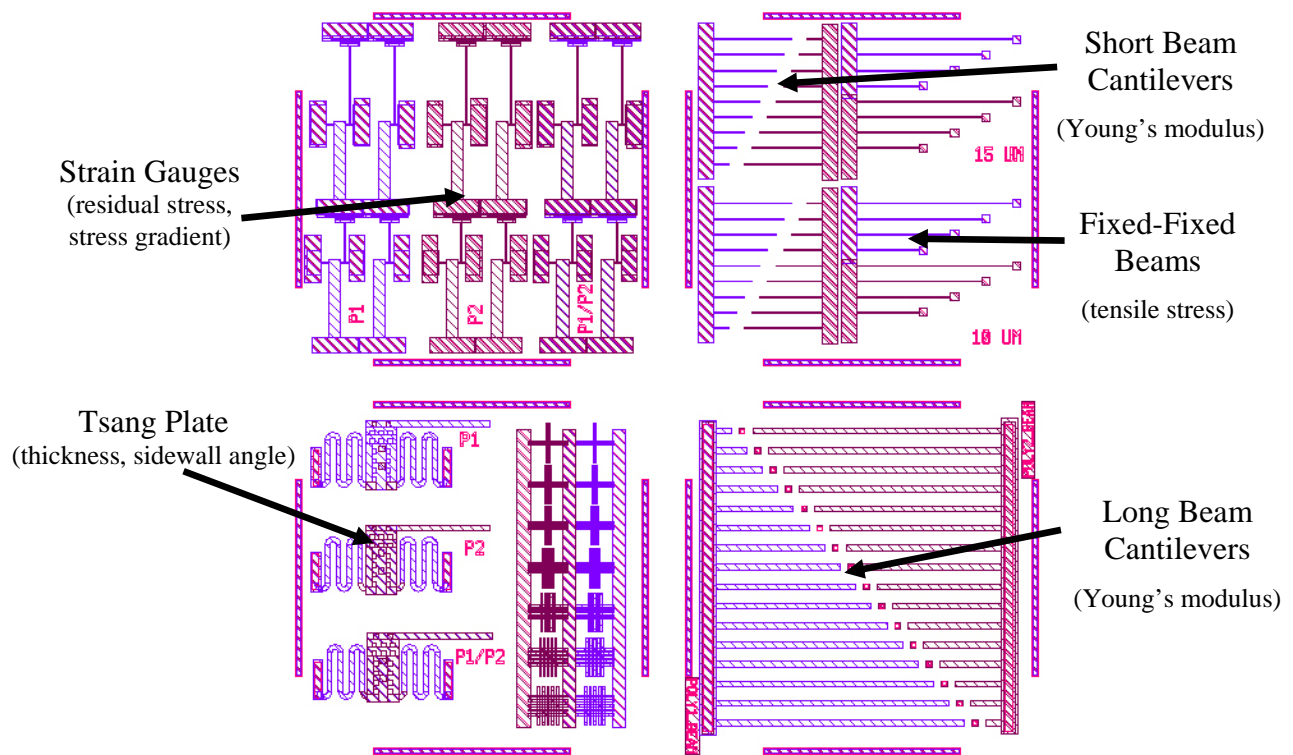


**Figure 9 - The full layout of the test die showing the structures and the resulting material properties measured.**

## 5. Software

Control of the piezoelectric actuator is accomplished through an NI LabVIEW control panel shown in Figure 10. The existing panel allowed for control of the waveform type, its amplitude, and DC offset. An additional panel was added which implemented automated frequency sweeping. This control allows the operator to select a start frequency, stop frequency, step size, and step duration. The code automatically detects a reverse sweep and the Reverse Sweep indicator LED lights up. The user is given the option to generate a log file for the frequency sweep which includes the start and stop times for each step in the sweep. This log file can be parsed by the imgFIX program to determine which image was captured at each frequency. This small C++ program compares the time stamps of the image files with those in the frequency sweep log file. The source code for this program has been included in Appendix A.

In order to better control the displacement of the piezoelectric actuator, an Amplitude Correction option is included, which reads the appropriate voltage needed at each frequency from an external file. The calculation of the output voltages is assumed to be done by the user beforehand. Due to the lack of equipment necessary to determine the displacement of the actuator, this option was not used in this project. Access to a laser doppler vibrometer could enable this in the future. The total number of steps and their duration is shown in the indicators at the top-right corner of the GUI. During the sweep, the current frequency and amplitude are also shown in this area. The output used to generate the log file is shown in the bottom-left of the GUI.

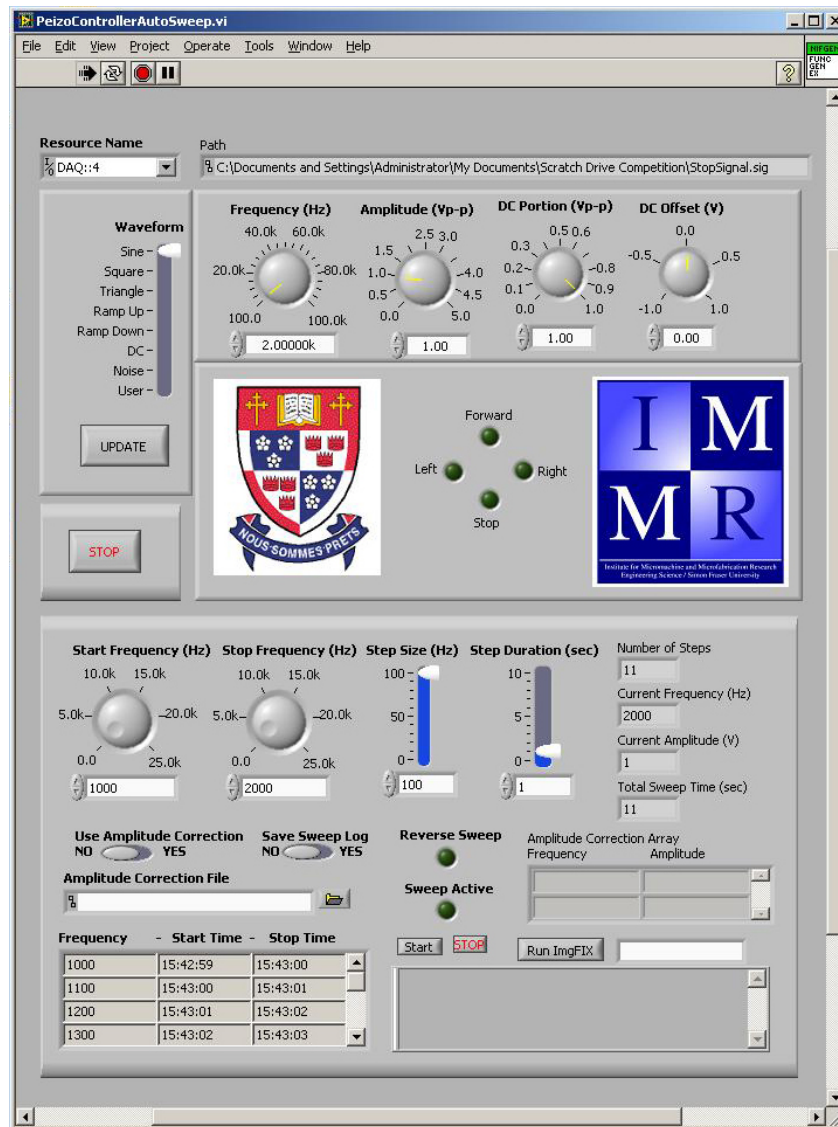


**Figure 10 - A screenshot of the frequency sweep control program.**

LabVIEW source code written by See-Ho Tsang provides the ability to use a gaming controller when doing manual testing of test structures. The program has mapped the joystick to frequency control, left side buttons to DC portion control, and the trigger buttons to amplitude control. The step size for each button press must be adjusted through modifying the appropriate variables in the source code.





**Figure 11 - A screenshot of the Vision inspection used to determine physical dimensions.**

The physical dimensions and resonance frequency of each test structure are determined using the NI Vision image analysis program. Images are loaded into an inspection script which outputs the length and width of each beam in pixels, shown in Figure 11. A different inspection script is used for each group of structures. Images are converted to gray, after which the caliper function is used to determine lengths and widths of each structure in pixels. The caliper function can produce varying results unless the imaging



conditions are constant. The parameters of the function must often be adjusted from run to run. By executing an automated inspection, an output log file is created which contains the name of the image and the measurement results. The inspection is able to detect the amplitude response of each beam as shown in Figure 12. The background specks seen in this image are discussed later in Chapter 6. Since the exposure time at each position of motion is smaller than that of the static structures, the image intensity of the moving parts is also smaller. Thus a lower intensity threshold must be used for the resonance frequency detection.

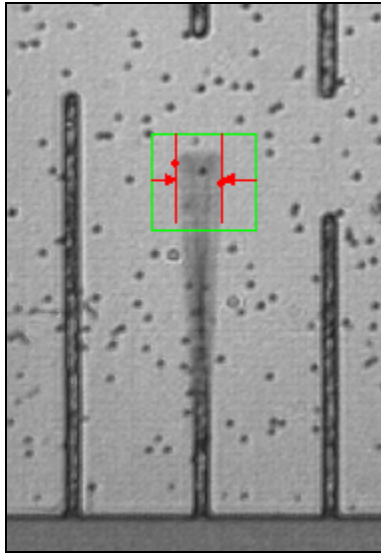


**Figure 12 - Measuring the amplitude of oscillation using Vision's caliper function.**

The log file is parsed and imported into MS Excel where the analysis is finalized. The Excel spreadsheet requires values for density, thickness of each layer, scaling parameters, and negative sidewall angle before outputting the final values.

## 6. Operational Procedure

This section outlines the current operational procedure for testing a wafer's parameters. Once a wafer has been fabricated, the test die is removed and placed in the holder attached to the piezoelectric actuator. The operator aligns the camera such that the bottom-left corner of the anchor for the set of structures to be tested matches the bottom-left corner of the image being captured. This alignment ensures that the test structures are within the proper regions of interest set in the Vision scripts. Orientation around the die can be determined by looking at the identification numbers found at the center of the die and along the top edge. The range for the frequency sweep is selected based on values given in Appendix B. The camera software, Motic Images Advanced 3.0, is then started and told to capture images automatically at an interval equal to the step duration variable. A step size of 100 Hz provides sufficient resolution for most measurements. The sweep is started several seconds after the camera capture sequence has begun. Once completed, LabVIEW will prompt the operator for a location and name for the log file. This process is then repeated for each group of structures to be tested, as shown in Figure 13.

In order to synchronize each image with the actuation frequency, the imgFIX program is called from the command line with the name of the log file passed into the program as the first parameter. This program compares the timestamp of each file having a TIFF extension in the execution directory with the start and stop times for each step in the log file. When a match is made, the image is copied into a sub-folder named sweep\_images and renamed to the appropriate frequency value.

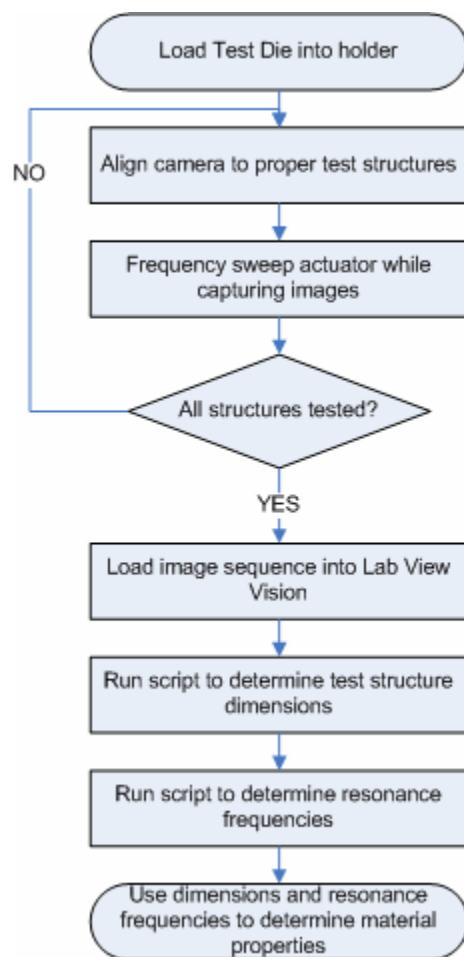


**Figure 13 - High level overview of the testing procedure.**

The set of images generated is loaded into Vision inspection to determine the frequency at which the amplitude is maximized. Since SU-8 is a transparent polymer, the sacrificial layer was roughened using an acetate mask, which greatly increased visibility, but added many tiny specks on the substrate. These can clearly be seen as black dots in both Figure 11 and Figure 12. Unfortunately, these dots interfere with Vision's caliper function giving incorrect measurements. An adequate solution for dynamically dealing with the dots has not yet been found. The region of interest for the caliper function is adjusted to exclude any dots

which are interfering with the edge detection. Adjusting the caliper's other settings, such as increasing the threshold and decreasing the sharpness, can help reduce this issue.

The thickness of the two layers, Poly1 and Poly2, is determined by using the pop-up structures seen in the bottom left corner of Figure 9. The structures are pushed up by pressing against the bottom of the main plate with a needle until the plate is perpendicular to the substrate. A beam is attached to the top of the plate which can now be examined edge on. The thickness is found by taking images of the edge of each corresponding pop-up structure with the 25x objective. Its variation around the wafer is quite uniform since SU-8 is a self-planarizing resist. Because the SU-8 resist is spun on, the edge bead effect causes the thickness to be slightly larger close to the wafer's edge.

In order to find the physical dimensions of each test structure, the higher resolution Big Catch EM-500M eyepiece camera is used. Using the same alignment procedure as described above, a high resolution image of each set of test structures is taken. Beam length can be found with a single 2.25x image for each group of beams. Beam width uses individual 25x images for each beam. These are loaded into a Vision script which determines the width and length of each structure using the built in caliper function, as shown in Figure 11. These data are then imported into an Excel spreadsheet or Matlab, where the values given in pixels are converted to microns using the scaling parameters shown in Table 6 and Table 7. The final step is to calculate Young's modulus or tensile stress using Equation 6 or 8.

The entire procedure currently requires about 30 minutes for each group of structures tested. Integration of a controllable X-Y stage will enable faster testing in the future.

## 7. Sources of Error

### 7.1. Non-Linear Duffing Effect

The non-linear behavior known as the Duffing effect can be observed once the input amplitude is increased beyond a certain level. This effect causes a hysteresis to form in the frequency response curve, as apparent in Figure 14. Due to this hysteresis, a balance must be made between avoiding the Duffing effect and being able to easily capture the response with the camera.

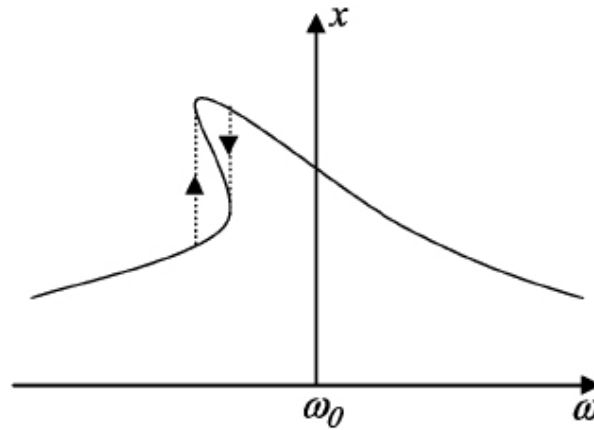


**Figure 14 - The frequency response of a cantilever operating in the non-linear region, image courtesy of V. Kaajakari, T. Mattila, A. Oja, and H. Seppä [7] .**

Non-linear behavior was observed in the fixed-fixed beams when the piezo actuator was driven with voltages over 100 V. This effect was not observed with the fixed-free beams, where applied voltages over 500 V caused no noticeable changes. When non-linear effects are present, the response of the beam will suddenly reduce to nearly no motion at a certain frequency. Normally, a smooth increase and decrease in response is observed. In the future, by measuring this effect, higher order terms for beam stiffness may be obtained.

## 7.2. Negative Sidewalls

The SU-8 process causes a negative sidewall effect on the fabricated structures as shown in Figure 15. Sidewalls are primarily caused by the diffraction of the exposure light propagating into the film [8] , which leads to beams with trapezoidal rather than rectangular cross-sections.

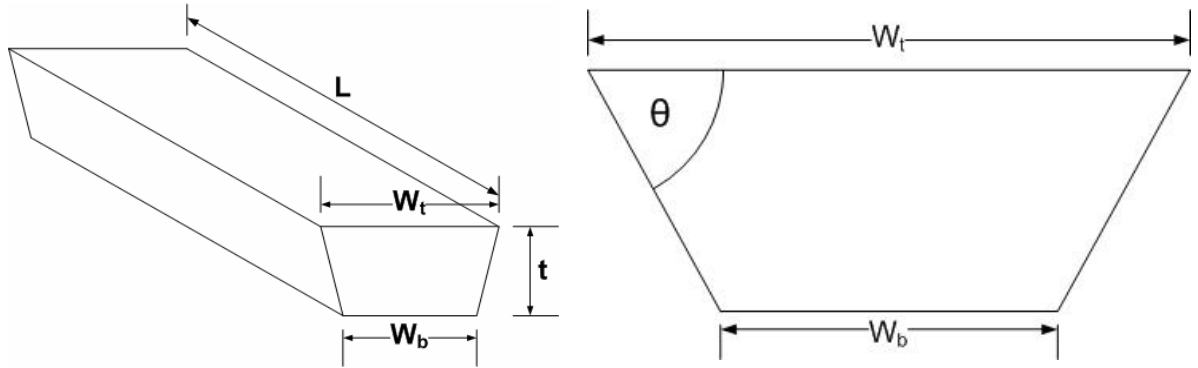


**Figure 15 - A beam with trapezoidal cross-section.**

Applying the in plane trapezoidal moment of inertia [9] to Equation 6, the corrected resonance frequency is given by

$$\omega = C_n \sqrt{\frac{E \cdot (W_b^3 + W_b^2 \cdot W_t + W_b \cdot W_t^2 + W_t^3)}{12 \cdot \rho \cdot L^4 \cdot (3W_b + W_t)}} , \quad (12)$$

where  $W_b$  is the bottom width and  $W_t$  is the top width respectively. Two different methods can be used to determine  $W_b$ . The sidewall angle ( $\theta$ ) can be found by pushing up one of the popup structures and examining the edge. Then the angle is measured using a Vision script, as shown in Figure 16. Because the structures are transparent, a second method is to measure  $W_b$  and  $W_t$  directly by focusing the microscope on the bottom and top surfaces of the structure. This method requires the use of an objective with a short depth of field, as

discussed in the next section. The negative sidewall angles measured throughout the test wafer are shown in Table 9.

**Table 9 - Negative sidewall data for different dies and test structures.**

Test Die #	Layer	Structure	Sidewall Angle ( $\theta$ )	Thickness ( $\mu\text{m}$ )	Baking Temperature ( $^{\circ}\text{C}$ )
30	Poly1	Pop-Up	85.5	18.3	120
30	Poly2	Pop-Up	86.5	38.0	120
45	Poly1	Pop-Up	73.1	18.4	120
45	Poly2	Pop-Up	77.3	40.0	120
31	Poly1	Pop-Up	-	16.9	95
22	Poly1	Long Beams	81.5	*	120
22	Poly2	Long Beams	84.6	*	120
29	Poly1	Long Beams	85.4	*	120
31	Poly1	Long Beams	87.9	*	95
32	Poly1	Long Beams	85.7	*	95
38	Poly1	Long Beams	83.8	*	120
30	Poly1	10 $\mu\text{m}$ Short Beams	86.3	*	120
38	Poly1	10 $\mu\text{m}$ Short Beams	85.6	*	120
38	Poly1	15 $\mu\text{m}$ Short Beams	86.5	*	120
38	Poly2	15 $\mu\text{m}$ Short Beams	85.7	*	120

\* Thickness can only be measured on the Tsang plate pop-up structures.

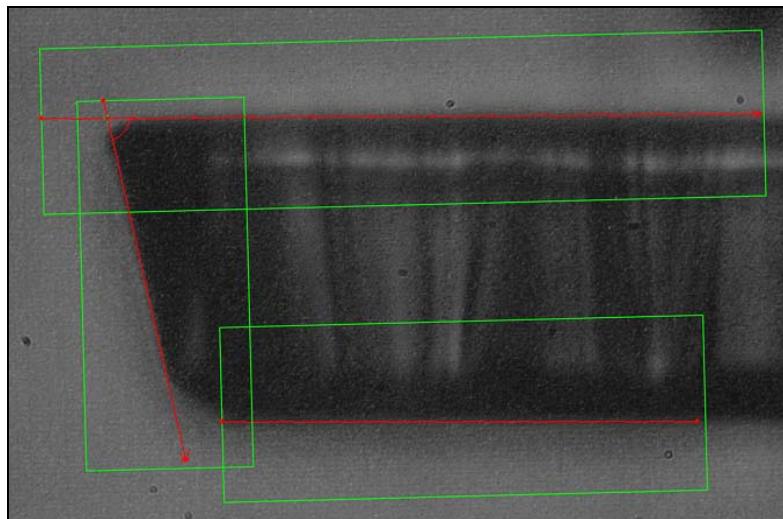


**Figure 16 - Measuring the negative sidewall using the pop-up structure and NI Vision.**

Taking the negative sidewall into account by using the trapezoidal Equation 12 instead of the ideal Equation 6 produces more accurate results. The error introduced into the calculated value of Young's modulus as a function of the sidewall angle is shown in Figure 17. As expected, the thicker Poly2 structures have nearly twice the error of their thinner Poly1 counterparts. The graph also shows that the thin low aspect ratio Poly1 Long Beams are the least affected by the negative sidewall issue and should produce the best results. Given that the average sidewall angle is around  $85^\circ$ , one could use the ideal formula together with data from only Poly1 structures to produce results with less than 6% error. Since sidewall angle measurements were obtained for most test structures, the trapezoidal formula was used throughout the rest of this project.

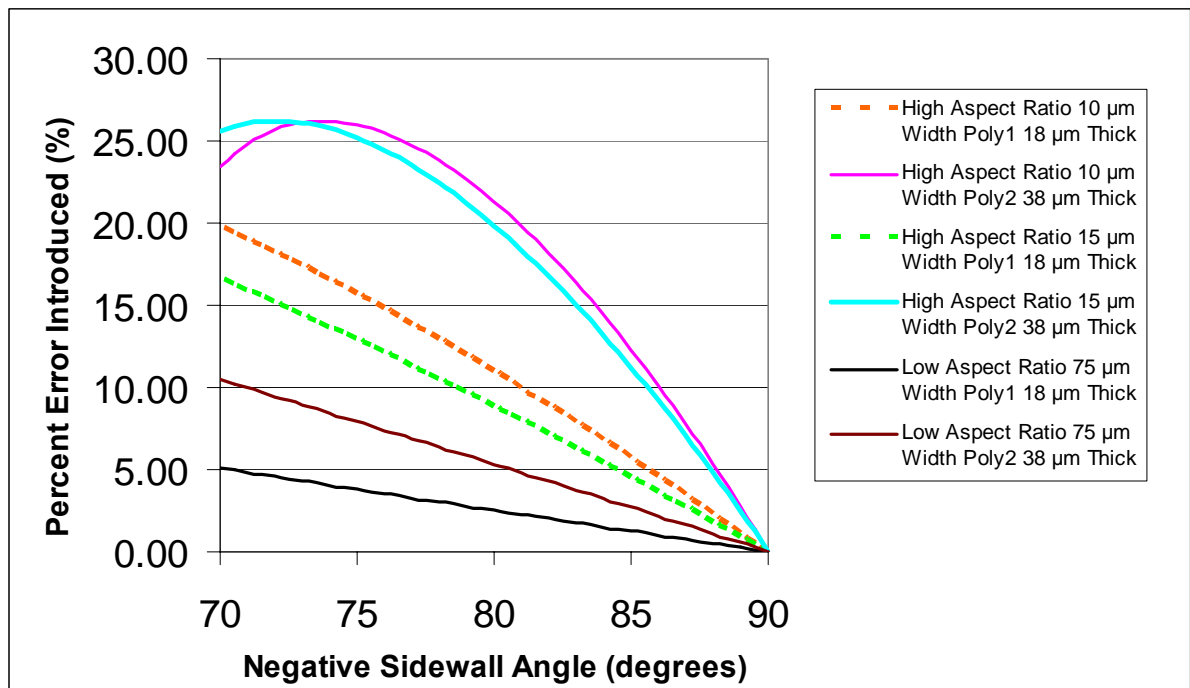


**Figure 17 - The error introduced into the value of Young's modulus calculated as a function of the sidewall angle.**



The penalty caused by uncertainty in the value of the negative sidewall angle can be seen in Figure 18. This uncertainty is estimated to be less than  $2^\circ$ , based on the distribution of measured values, corresponding to an error of about 2.5% in the calculated value of Young's modulus. As in Figure 17, the lowest errors correspond to the low aspect ratio structures.

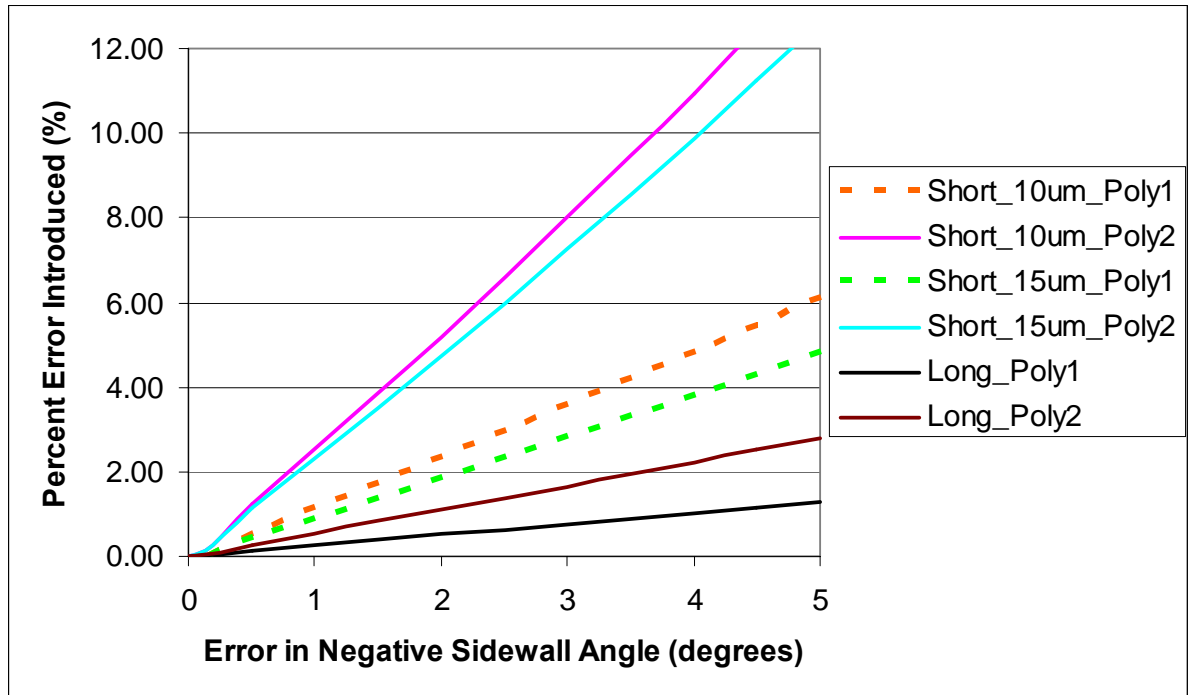


**Figure 18 - The error in calculated Young's modulus due to uncertainty in the value of the negative sidewall angle.**

### 7.3. Image Analysis

A large source of error in determining a test structure's physical dimensions arises from using image analysis. The microscope used in this project is equipped with 2.25x and 25x objectives. The length of test structures is determined with the 2.25x objective due to its large field of view. On the fixed ends, the length measurement starts from the black line on the edge of the anchor. At the other side, the length measurement finishes at the tip of the rounded end, as shown in Figure 19.

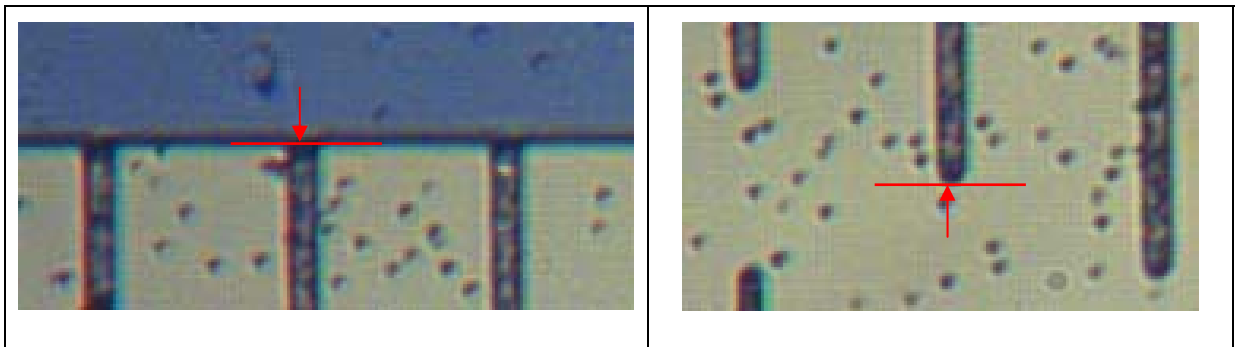


**Figure 19 - The start of the length measurement at the fixed end where beams are attached to the anchor is shown on the left. The end of the measurement at the rounded free ends is shown on the right.**

In addition to changing the objectives, magnification can also be adjusted through a knob herein referred to as the eyepiece zoom. The error caused by a mistake of several pixels in the length measurement for two types of beams is shown in Figure 20 and Figure 21. The low aspect ratio Long Beams have about half the error of the Short beams, since the error is a much smaller percentage of the overall length.

Proper measurement of the width can minimize the largest source of error in the image analysis. Because the widths range from 10  $\mu\text{m}$  to 75  $\mu\text{m}$ , a single pixel mistake introduces a large error at the 2.25x magnification, as shown in Figure 22 and Figure 23.

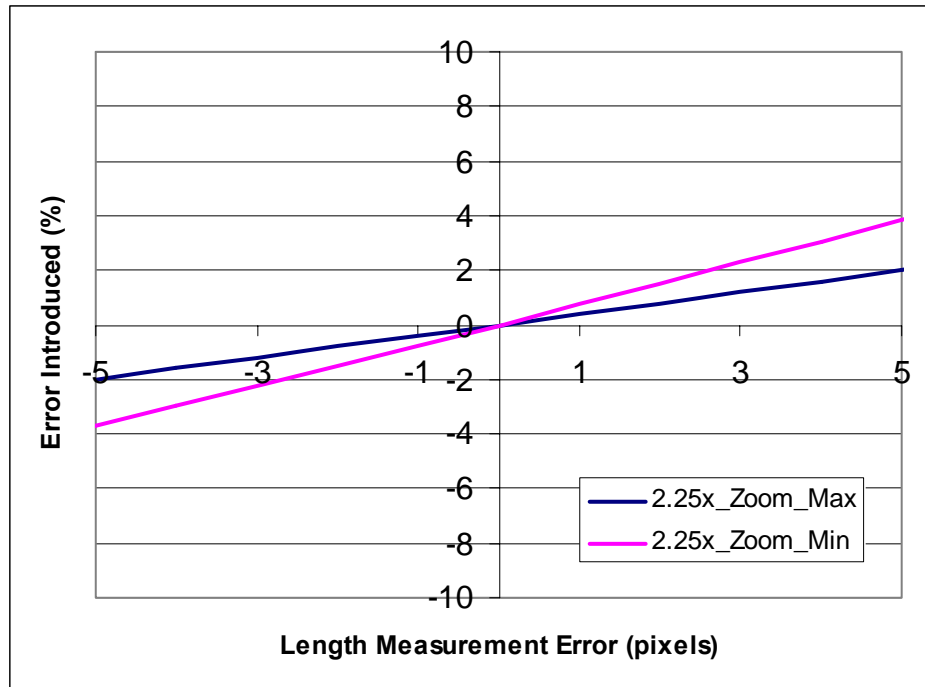


**Figure 20 - The error introduced into the calculated value of Young's modulus by an error of several pixels in the length measurement of an 1800  $\mu\text{m}$  Long Beam.**

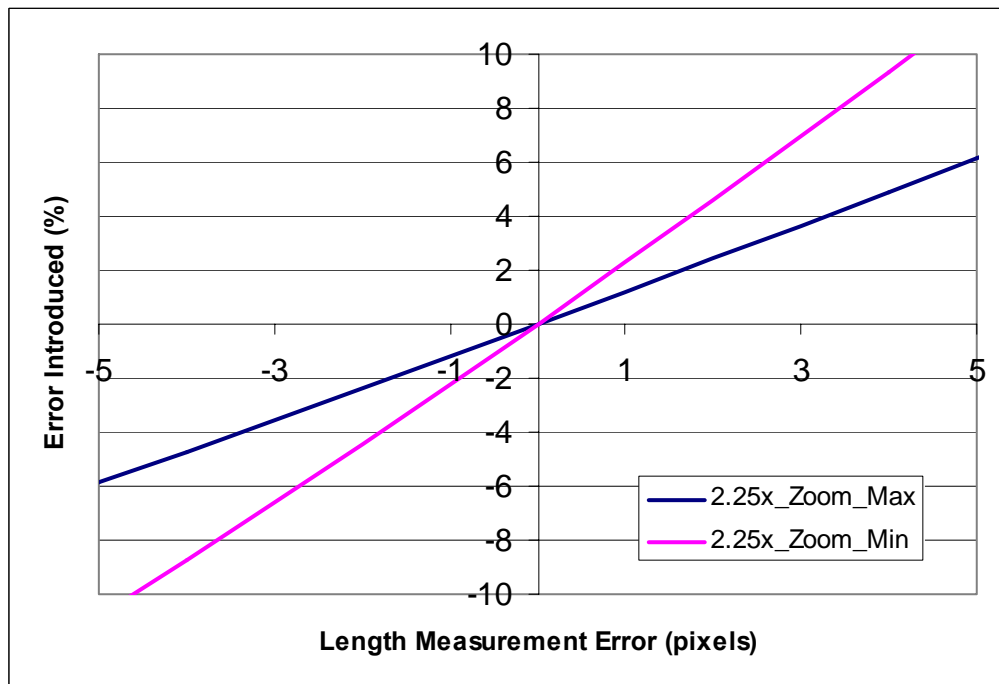


**Figure 21 - The error introduced into the calculated value of Young's modulus by an error of several pixels in the length measurement of a 600  $\mu\text{m}$  Short Beam.**

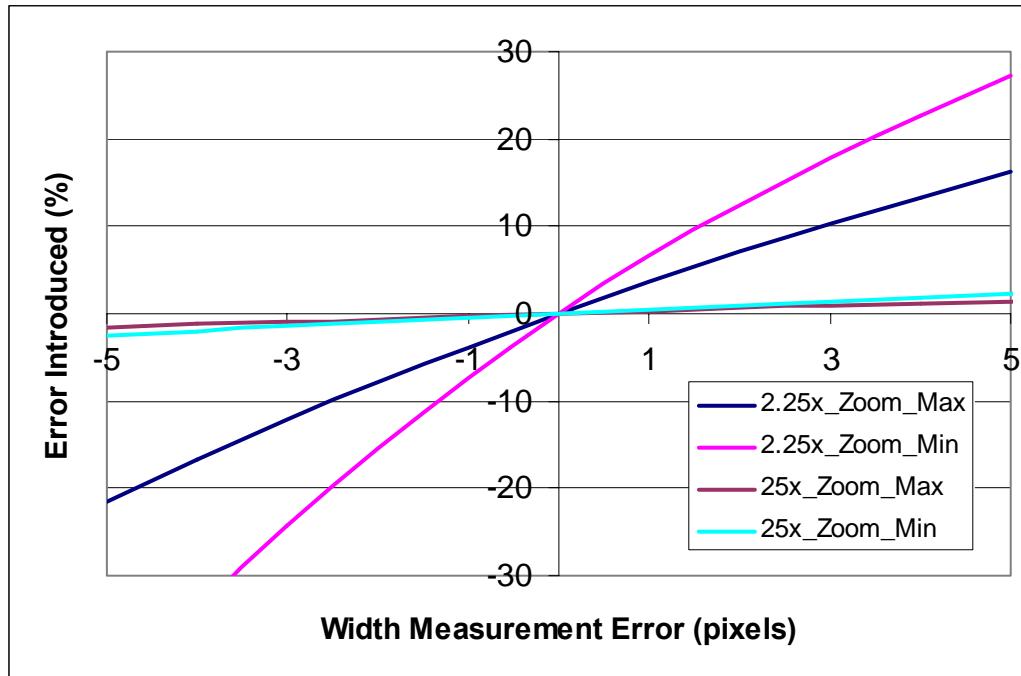


**Figure 22 - The error introduced into the calculated value of Young's modulus by an error of several pixels in the width measurement of an 1800  $\mu\text{m}$  Long Beam.**

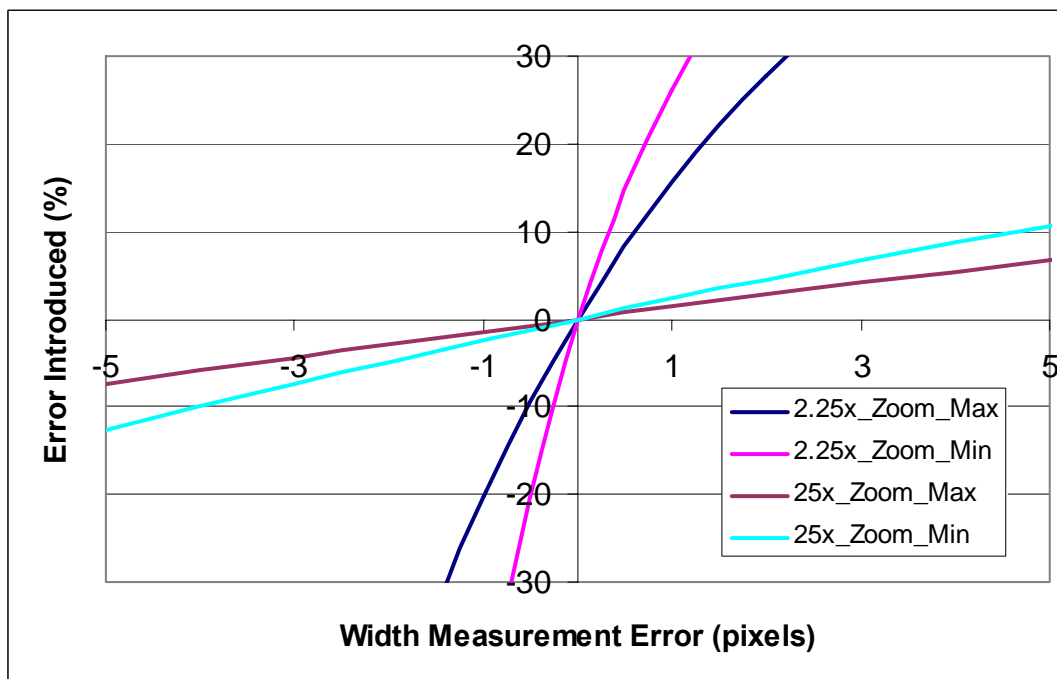


**Figure 23 - The error introduced into the calculated value of Young's modulus by an error of several pixels in the width measurement of a 600  $\mu\text{m}$  Short Beam.**

All of the widths used can fit within the higher power objectives' field of view.

Unfortunately, using the 25x objective does not significantly improve the situation. Instead of appearing sharp, the sidewall causes the edge to appear blurry, as apparent in Figure 24.

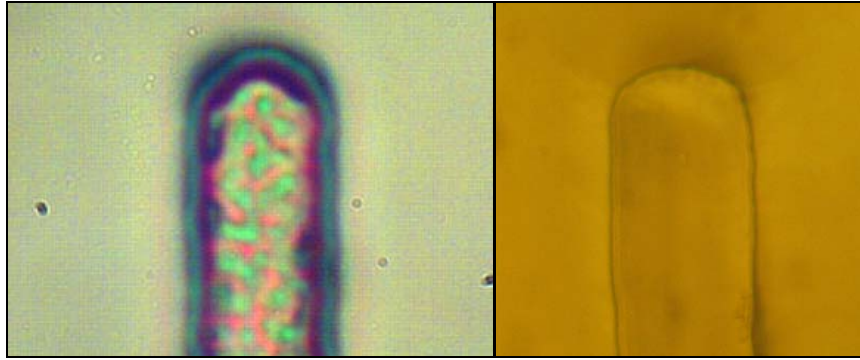


**Figure 24 – Left: A 15  $\mu\text{m}$  beam as seen with a 25x objective. The edges appear out of focus due to the sidewall. Right: The same beam observed using a 50x objective.**

This blurring can be resolved by using an objective with a small depth of field, given by

$$DOF = \frac{\lambda \sqrt{n^2 - (NA)^2}}{(NA)^2}, \quad (13)$$

where  $NA$  is the objective's numerical aperture,  $n$  is the index of refraction of the medium, and  $\lambda$  is the wavelength. A second microscope with 50x and 80x objectives was used for width measurements. The depth of field for each objective is given in Table 10. Over 200 measurements were made with an eyepiece micrometer attached to the second microscope under 80x magnification. The amount of sidewall apparent in the field of view is graphed

**Table 10 - Depth of field for different power microscope objectives.**

Depth of Field ( $\mu\text{m}$ )	Objective	Numerical Aperture
347	2.25x	0.04
5.5	25x	0.31
0.81	50x	0.70
0.65	80x	0.75

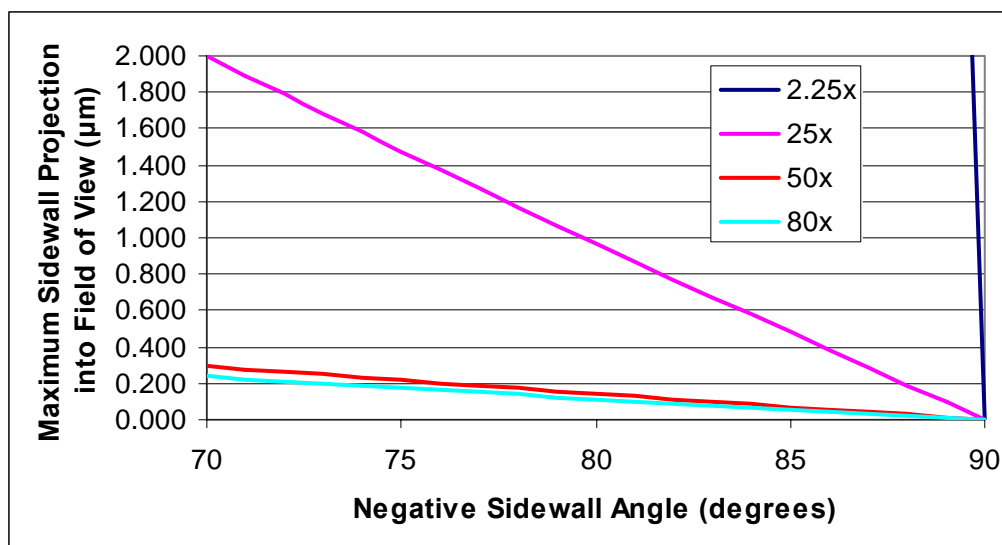


**Figure 25 - The maximum in plane projection of the sidewall as a function of the sidewall angle.**

in Figure 25, which shows a six fold improvement if a 50x objective is used instead of the 25x objective.

## 7.4. Density

Lastly as outlined in Figure 26, the value of density used presents a small source of error. A value of  $1200 \text{ kg/m}^3$  was used throughout the calculations in this project.

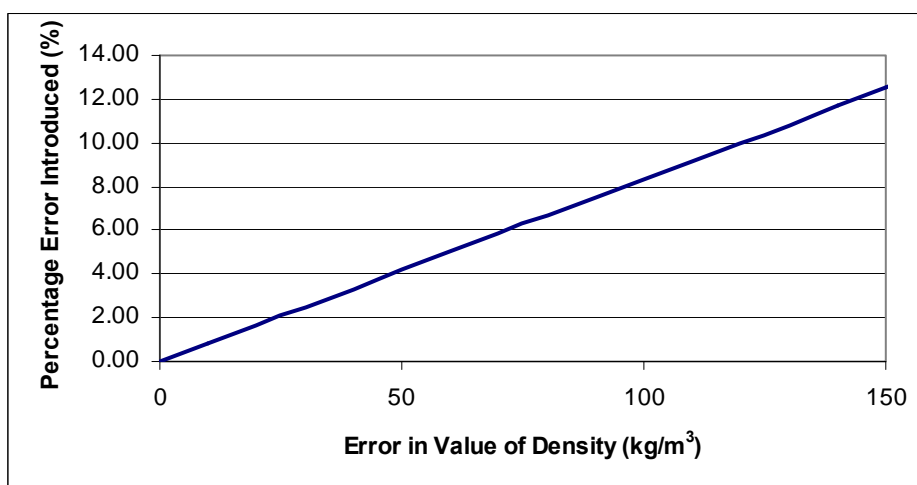


**Figure 26 - The error of a mismatch between the real density and the value used.**

## 8. Results

Two wafers with 52 1x1cm test dies each were fabricated by Dan Sameoto using his SU-8 rapid prototyping process [6]. The first wafer, fabricated with a polystyrene sacrificial layer, was not testable because structures were curling down against the substrate. The second wafer used ProLift, a polyimide based resist, as a sacrificial layer, with better results. Although the features had swollen to twice their design size, very few structures were stuck. The feature swelling was due to bad contact with the emulsion mask used during exposure. The bad contact issue will be addressed in the future by switching to more expensive chrome masks, which are not flexible. Half of this wafer was baked at 120°C while the other half was baked at 95°C, after the wafer was cut in half. The distribution of the dies around the wafer and the location of the dies tested are shown in Figure 27. The dies tested were all from the wafer's center area, containing the best structures fabricated. Due to the feature swelling, no useful data on the tensile stress could be extracted from the fixed-fixed beams on any die. Further discussion of fabrication issues will be available in Dan Sameoto's PhD thesis, to be published shortly.

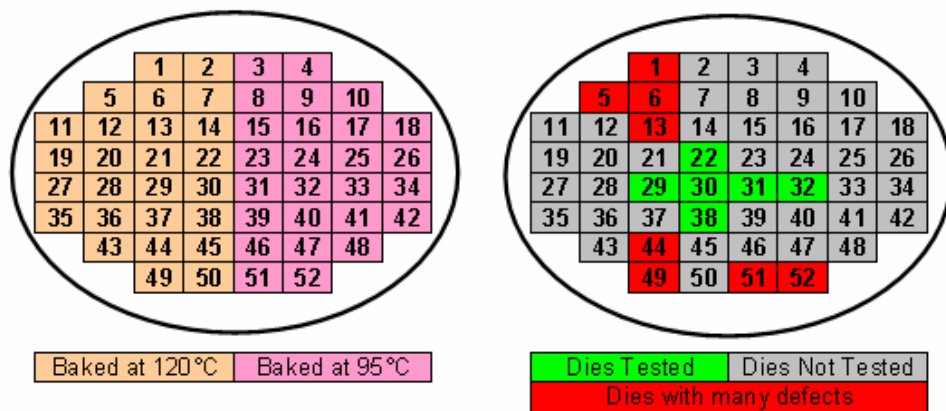


**Figure 27 - The layout of the test dies around the wafer, their baking temperature on the left. The dies tested and the dies with defects on the right.**

## 8.1. Young's Modulus

A total of six test dies with 90 structures were tested, out of which four were baked at 120°C and the others at 95°C. The calculated values of Young's modulus along with their standard deviations are shown in Table 11.

**Table 11 – The values of Young's modulus calculated from the four 120°C test dies.**

	Design Width		Test Die ID#	22	38	30	29	Weighted Mean
Short Beam	10µm	POLY1	Young's Mod (GPa)	broken	3.99	4.04	stuck	4.02
			Std (GPa)		0.17	0.11		0.04
			# samples		2	2		4
		POLY2	Young's Mod (GPa)	broken	stuck	stuck	stuck	
			Std (GPa)					
			# samples					
	15µm	POLY1	Young's Mod (GPa)	3.59	3.84	3.86	stuck	3.76
			Std (GPa)	0.14	0.19	0.46		0.15
			# samples	5	5	4		14
		POLY2	Young's Mod (GPa)	3.80	3.72	4.12	stuck	3.90
			Std (GPa)	0.07	0.09	0.09		0.21
			# samples	5	2	4		11
Long Beam	POLY1	Young's Mod (GPa)	3.84	3.85	3.97	3.90	3.90	
		Std (GPa)	0.08	0.22	0.16	0.06	0.06	
		# samples	3	4	7	9	23	
	POLY2	Young's Mod (GPa)	3.72	stuck	4.06	stuck	3.92	
		Std (GPa)	0.16		0.24		0.24	
		# samples	2		3		5	
TOTAL SAMPLES								57

These results are on par with values found in literature, which are listed in Table 12. While these values should not be compared directly due to differences in manufacturing processes and SU-8 formulations used, they provide a range of expected values. Since the data from the Poly1 Long Beam structures were shown in the sources of error section to be the most reliable, the value of Young's modulus on the 120°C half of the wafer is concluded to be  $3.90 \pm 0.06$  GPa. If all of the results are included, the final value comes out to  $3.88 \pm 0.20$  GPa.



**Table 12 - A list of values for the Young's modulus of SU-8 found in publications.**

Range of SU-8 Young's modulus (GPa)	Uncertainty (GPa) (if provided)	Measurement Method	Year	Reference
3.8 - 5.4	-	Laser Acoustic	2004	[10]
2 - 3	0.5	Contact surface profilometer beam	2005	[11]
2.5 - 2.7	-	Screw Driven Tensile Test	2003	[12]
4.02	-	Screw Driven Tensile Test	1997	[13]
4.95	0.42	Beam Deflection Test	1998	[14]

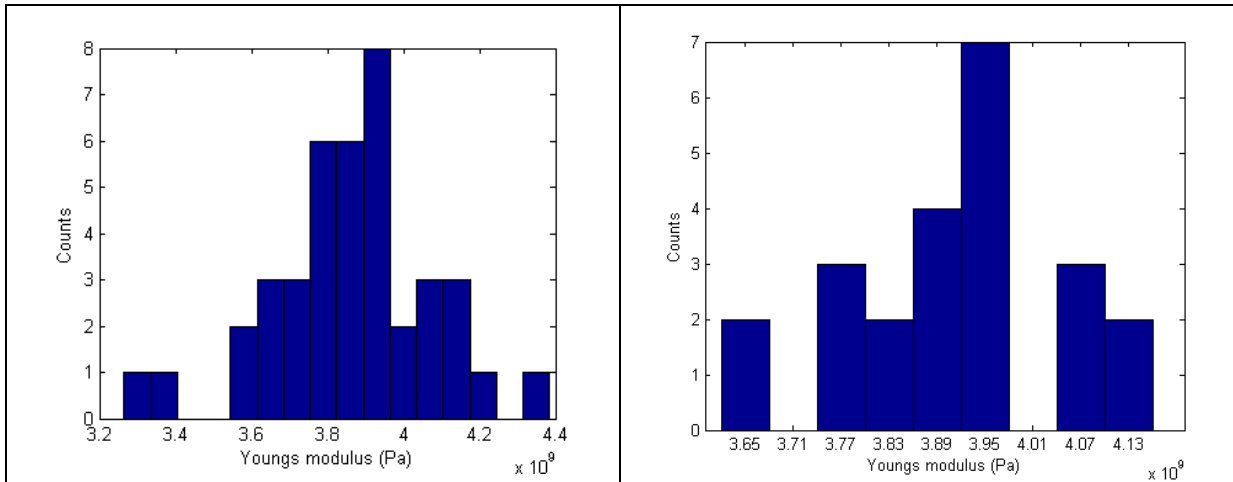


**Figure 28 - Distribution of Young's modulus from the all of the structures on the 120°C test dies is shown on the left and just the data from Long Beams on the right.**

Comparing the distribution of results shown in Figure 28 from all test structures with just the data from the Long Beam sets, a smaller standard deviation with fewer outliers is seen in the latter. The impact of the negative sidewall on the beam response is most evident in Figure 29 and Figure 30. The former shows experimental data, while the latter shows the predicted behavior for a constant negative sidewall angle of 86°. As expected, the change in response as a function of thickness is greater for the high aspect ratio Short Beams.

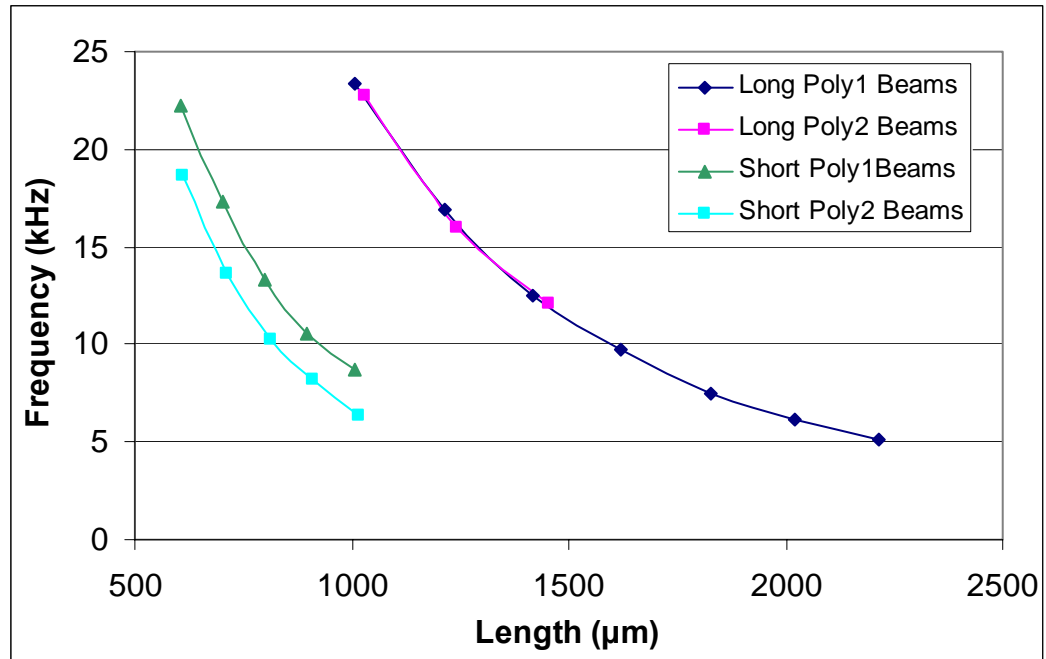


**Figure 29 - The experimentally observed differences between the behaviour of Poly1 and Poly2 beams within a set of Long Beams and a set of Short Beams.**

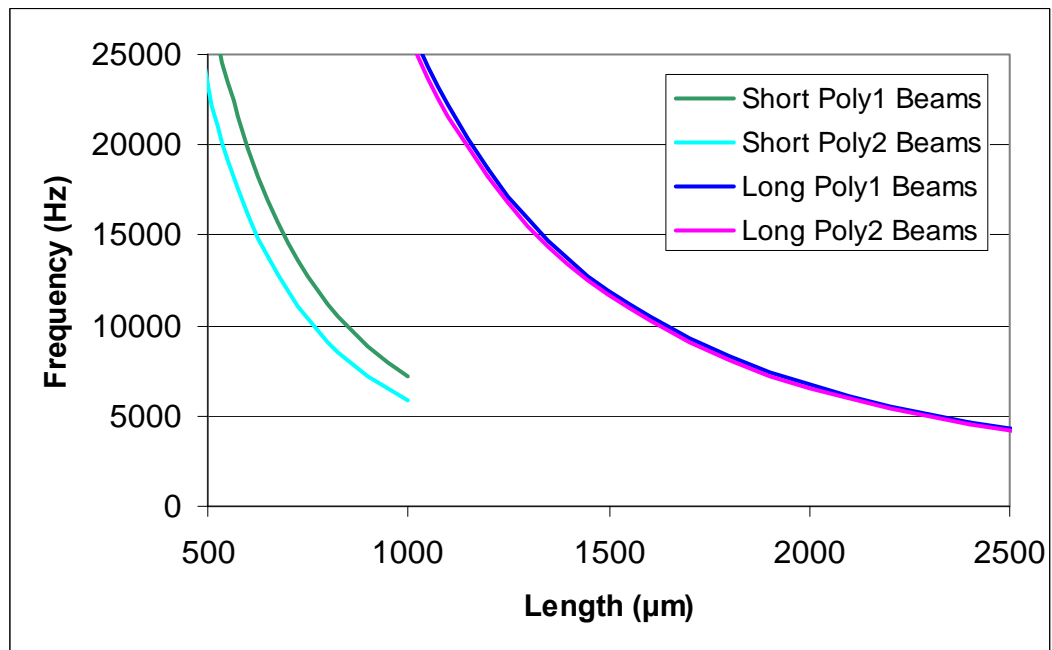


**Figure 30 - Theoretical predictions of the behaviour of the same test structures presented in Figure 29.**

**Table 13 - The values of Young's modulus calculated from the two 95°C test dies.**

	Design Width		Test Die ID#	31	32	Weighted Mean
Short Beam	10um	POLY1	Young's Mod (GPa)	4.47	4.11	4.33
			Std (GPa)	0.08	0.05	0.25
			# samples	3	2	5
	POLY2		stuck	stuck		
	15um	POLY1	Young's Mod (GPa)	4.33	4.16	4.22
			Std (GPa)	0.02	0.28	0.12
			# samples	2	4	6
	POLY2		stuck	stuck		
	Long Beam	POLY1	Young's Mod (GPa)	3.98	3.92	3.95
Std (GPa)			0.08	0.13	0.04	
# samples			10	12	22	
POLY2			stuck	stuck		

**TOTAL SAMPLES** **33**

The results from the two 95°C test dies are shown in Table 13. At first glance, the results appear to indicate that the lower baking temperature caused an increase in the Young's modulus. Further investigation revealed that the test structures on the 95°C portion of the wafer had significant curl, although most were not touching the substrate. The effects of this curl on the analysis will be investigated in the future. Note that the results produced by the Long Beams are within the uncertainty of their 120°C counterparts.

**Table 14 - Curve fits for the four sets of Long Beams.**

Test Die #	29	30	31	32
<b>E (GPa)</b>	3.94	3.99	4.03	4.00
<b>Reduced <math>\chi^2</math></b>	0.95	0.94	0.98	0.72
<b>Std (GPa)</b>	0.04	0.08	0.04	0.09
<b>Baking Temperature (°C)</b>	120	120	95	95

One of the goals of this project was to ensure the testing was as rapid as possible. In order to facilitate this goal, the minimum number of structure groups required to produce good results was determined. Because Long Beam structures have been shown to provide the

best data, non-linear fits used sets of Long Beams which had more than five samples. The non-linear least squares fits, with Equation 12, were implemented in Matlab using functions provided in the Curve Fitting Toolbox. The results of these fits are shown in Table 14, and one curve fit is presented in Figure 31. The values of Young's modulus extracted were compared with the results given by the full analysis. On average, the values given by the curve fits were within 0.06 GPa of the values calculated using the full analysis, which implies that all of the necessary data can be extracted using just a set of Poly1 Long Beams with more than 5 samples. No additional data is provided by testing the Short Beam groups.

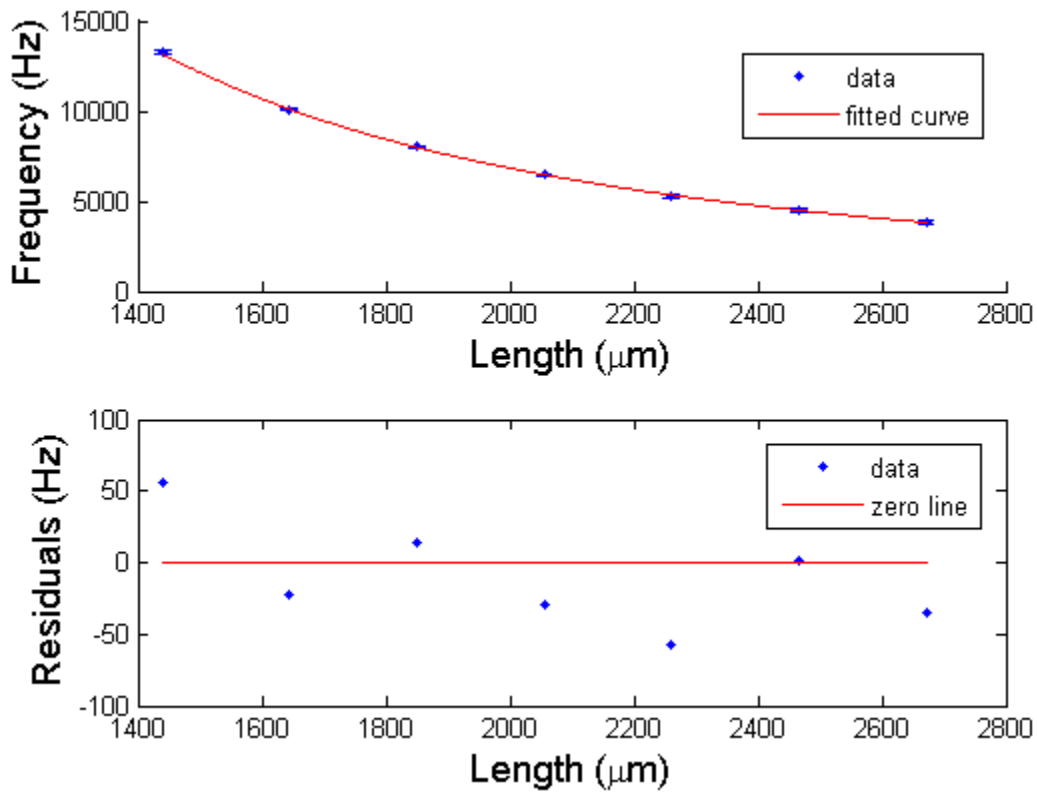


**Figure 31 - A non-linear curve fit using one set of Poly1 Long Beams.**

## 8.2. Error due to Operation in Air

In order to quantify the amount of damping introduced by operating in air rather than in vacuum, the response of three beams was measured one week after fabrication. Figure 32 shows these results. Another beam from a test die baked at 95°C was characterized to determine the effect of curling on beam response. Their Q factor was calculated and Equation 10 was used to find the damping ratio in each case.

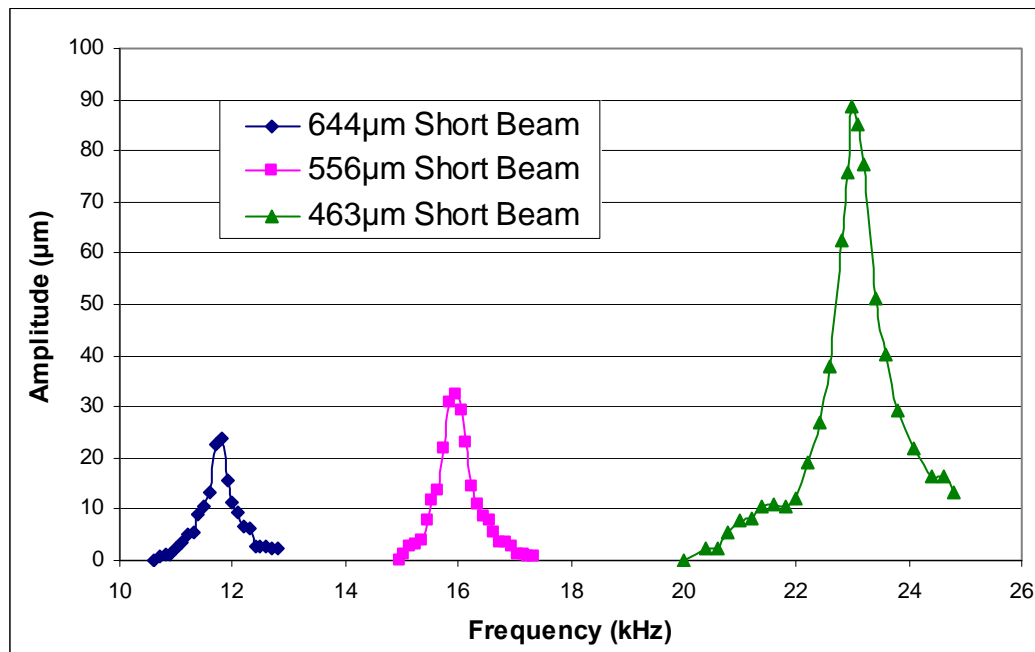


**Figure 32 - Response of three Short Beams of varying length.**

The error introduced by operating in air was calculated using Equation 9 and is shown in Table 15. Since all of the errors in the 120°C beam data are less than a hundredth of a percent, we conclude that no significant advantage would be gained by operating in vacuum. The 95°C beam showed the lowest Q factor, indicating that the curling degrades the response of the beam.

**Table 15 - The Q factors, damping ratio, and corresponding error for four beams.**

Baking Temperature (°C)	Width (μm)	Length (μm)	$f_d$ (Hz)	Q	$\zeta$	% error
120	23.6	644	11,700	51.3	0.0097	0.005
120	23.3	556	15,900	41.6	0.0120	0.007
120	23.2	463	22,800	48.8	0.0102	0.005
95	30.2	826	12,750	34.8	0.144	0.010

### 8.3. Sample Degradation

Ten weeks after fabrication, the response of the three 120°C beams was investigated once more. No measurable changes in any beam's Q factor was observed, as presented in Figure 33. This result is consistent with previous studies which showed that changes in the material properties of SU-8 are primarily due to the evaporation of solvent and occur within a few days after fabrication [12] .

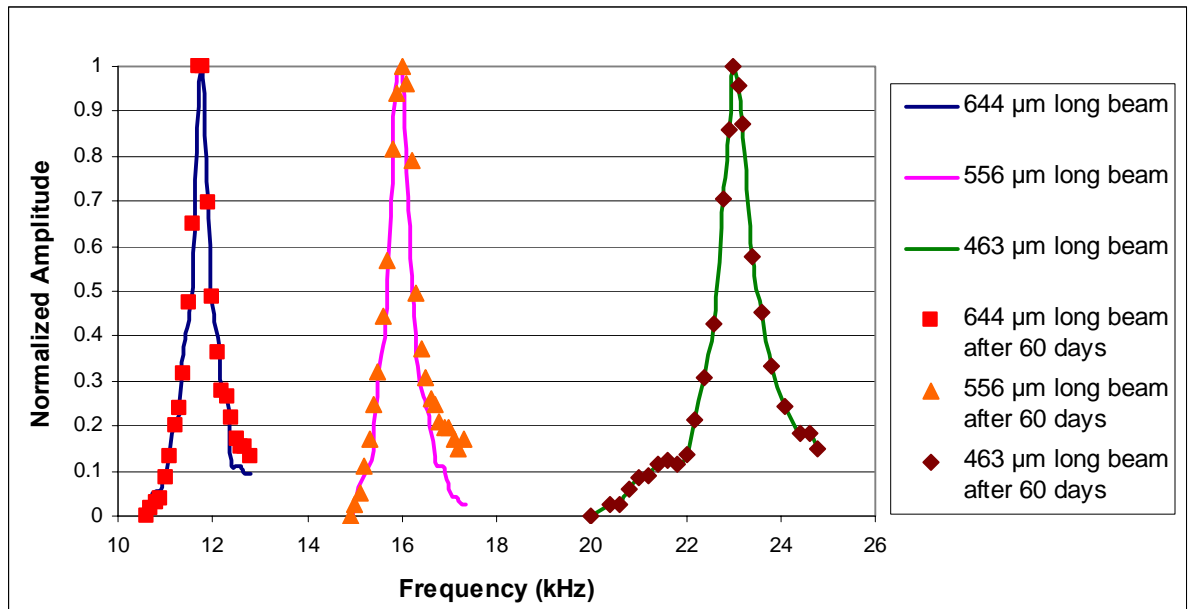


**Figure 33 - The normalized response of three beams one week and ten weeks after fabrication.**

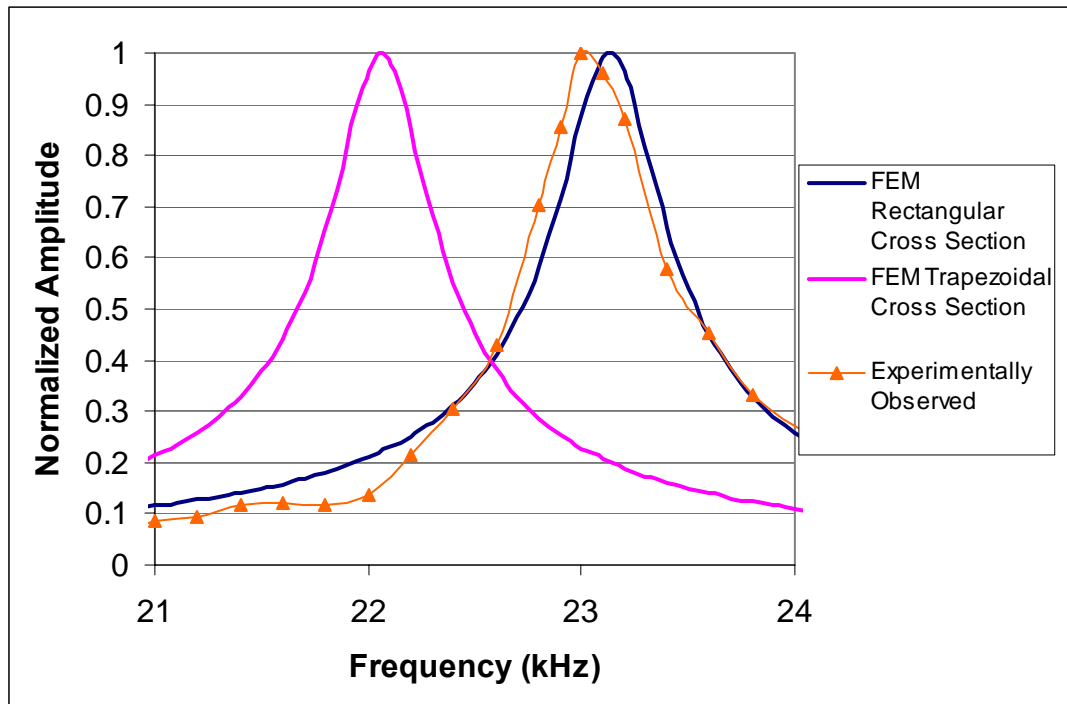
## 9. Finite Element Analysis

A finite element (FE) analysis of the test structures was completed with the software program ANSYS in order to evaluate its potential for aiding in test structure design and parameter testing. In addition to the density and Young's modulus values used in the previous section, the value of Poisson's ratio was assumed to be 0.22 [10] . The damping ratios were set to the calculated values shown in Table 15. Each beam model was made from 20 elements of the ANSYS Beam3 element type which allows translations in the x-y plane and rotations about the z-axis. Two models of each beam were created. One assumed no negative sidewall with a rectangular cross section, while the other used the experimentally measured sidewall angle corresponding to a trapezoidal cross section. Table 16 compares the modal frequencies produced by the FE analysis with the experimental measurements. Although the experimental results of all cases fell between the output of the trapezoidal model and the rectangular model, the latter provided closer results.

**Table 16 - A comparison of the modal frequencies calculated in Ansys and the experimental results.**

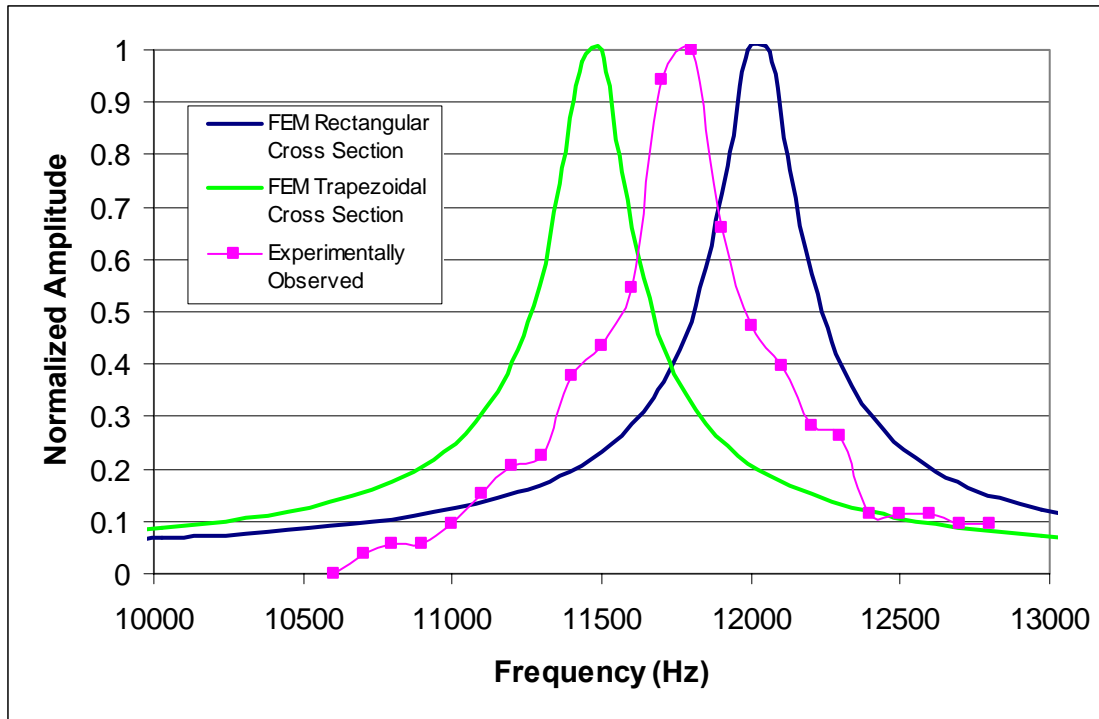
Test Die #	Data Source	Beam	Layer	Sidewall Angle	Mode 1	Mode 2
22	FEM Rectangular Cross Section	Long Beam 14	Poly2	90	3051	19099
	FEM Trapezoidal Cross Section			80.3	3003	18798
	Experimental Measurement			80.3	3040	18950
30	FEM Rectangular Cross Section	Short 15 $\mu$ m Beam 6	Poly2	90	23134	144703
	FEM Trapezoidal Cross Section			85.7	22061	138019
	Experimental Measurement			85.7	22800	-
	FEM Rectangular Cross Section	Long Beam 7	Poly1	90	6244	39043
	FEM Trapezoidal Cross Section			85.2	6165	38551
	Experimental Measurement			85.2	6170	-
	FEM Rectangular Cross Section	Short 15 $\mu$ m Beam 4	Poly2	90	12025	75283
	FEM Trapezoidal Cross Section			85.7	11469	71812
	Experimental Measurement			85.7	11700	-

Figure 34 and Figure 35 compare the beam response predicted by both models with the experimental data. As expected from the theory, an increased negative sidewall effect lowers both the mass and stiffness of a beam, with a larger reduction in the latter. This reduction causes the resonance frequency of the beam to decrease. The analysis was also used to determine the response for several different values of Young's modulus, as shown in Figure 36. Future improvements will include the use of curvature measurements and model elements with more degrees of freedom.



**Figure 34 - Experimentally observed response of Poly2 Short 15  $\mu\text{m}$  Beam 6, compared with the results of a harmonic analysis for both rectangular and trapezoidal cross sections.**





**Figure 35 - Experimentally observed response of Poly2 Short 15  $\mu\text{m}$  Beam 4, compared with the results of a harmonic analysis.**

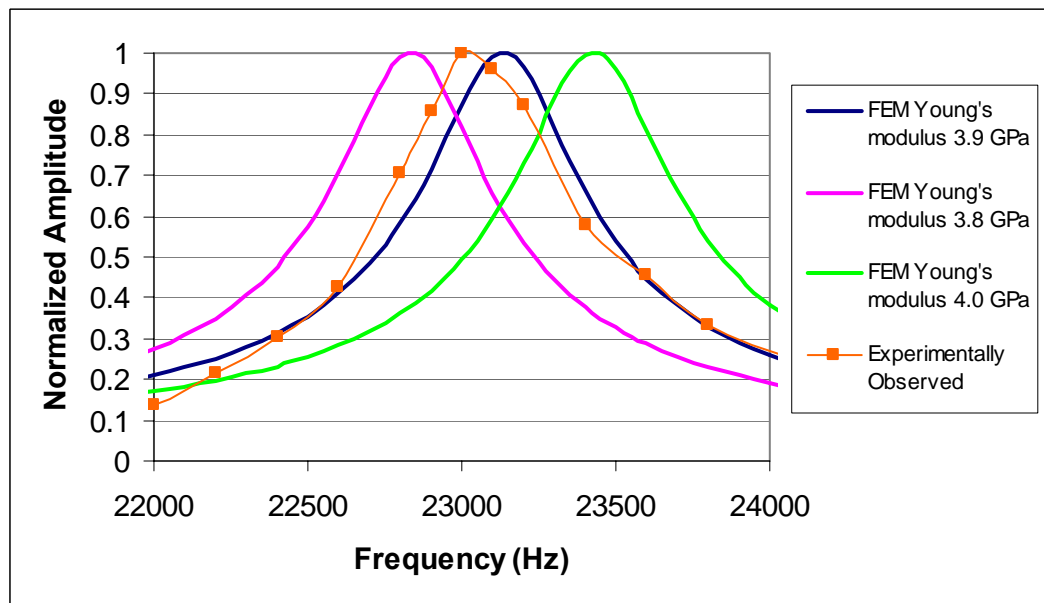


**Figure 36 - The FEM predicted response for three values of Young's modulus using the rectangular beam model and the observed response.**

## Conclusion and Future Work

A rapid measurement system for polymer material properties was built. The low cost system enables operators to track changes within processing runs. This system was used to determine a Young's modulus of  $3.90 \pm 0.06$  GPa within a SU-8 rapid prototyping process. The effects of manufacturing defects on the data analysis were examined in detail.

Future improvements to the system will allow a greater degree of automation. The integration of a controllable X-Y stage will decrease the testing time by removing the need for an operator to manually align the system. These stages would enable wafer level testing. Placing the system within an environmental chamber will provide insight into the relationship between material properties and parameters, such as humidity. Further finite element analysis will investigate the effect of curvature on the beam's in plane response. Finally, the results of testing different polymers will be used to optimize the test die layout.

## References

- [1] <http://www.mit.edu/~6.777/matprops/matprops.htm>, “6.777J/2.751J Material Properties Database”, Professors Carol Livermore and Joel Voldman, 2004.
- [2] V. T. Srikar and S. M. Spearing, “A critical review of microscale mechanical testing methods used in the design of microelectromechanical systems,” *Experimental Mechanics*, vol. 43, no. 3, pp. 238-247, September 2003.
- [3] Inman, Daniel. 2008. *Engineering vibration 3<sup>rd</sup> ed.* New Jersey: Pearson Education.
- [4] Ikeda, Takuro. 1990. *Fundamentals of Piezoelectricity*. London: Oxford University Press.
- [5] See-Ho Tsang. 2006. *Automated assembly of hingeless 90 degrees out-of-plane microstructures*. M.A.Sc. thesis, Simon Fraser University, Burnaby, BC.
- [6] Dan Sameoto, See-Ho Tsang, and M. Parameswaran, “Polymer MEMS processing for multi-user applications,” *Sensors and Actuators A: Physical*, vol. 134, no. 2, pp 457-464, 15 March 2007.
- [7] V. Kaajakari, T. Mattila, A. Oja, and H. Seppä, “Nonlinear limits for single-crystal silicon microresonators,” *IEEE Journal of Microelectromechanical Systems*, vol. 13, no. 5, pp. 715-724, October 2004.
- [8] Won-Jong Kang, Erik Rabe, Stefan Kopetz and Andreas Neyer, “Novel exposure methods based on reflection and refraction effects in the field of SU-8 lithography,” *J. Micromech. Microeng.*, vol. 16, pp. 821-831, 20 March 2006.
- [9] Jonathan W. Wittwer. 2005. *Simulation-Based Design under Uncertainty for Compliant MicroElectroMechanical Systems*. Ph.D. thesis, Brigham Young University, Provo, UT.
- [10] Hui Yu, Oluwaseyi Balogun, Biao Li, Todd W Murray and Xin Zhang, “Building embedded microchannels using a single layered SU-8, and determining Young's modulus using a laser acoustic technique,” *J. Micromech. Microeng.*, vol. 14, pp. 1576-1584, 9 August 2004.
- [11] Hopcroft M, Kramer T, Km G, Takashima K, Higo Y, Moore D and Brugger, “Micromechanical test of SU-8 cantilevers,” *Fatigue Fracture Eng. Mater. Struct.*, vol. 28, pp. 735–742, August 2005.

- [12] R Feng and RJ Farris, "Influence of processing conditions on the thermal and mechanical properties of SU8 negative photoresist coatings," *J. Micromech. Microeng*, vol. 13, pp. 80-88, January 2003.
- [13] H Lorenz, M Despont, N Fahrni, N LaBianca, P Renaud, and P Vettiger, "SU-8: a low-cost negative resist for MEMS," *J. Micromech. Microeng*, vol. 7, pp. 121-124, April 1997.
- [14] L. Dellmann, S. Roth, C. Beuret, G. Racine, H. Lorenz, M. Despont, P. Renaud, P. Vettiger, and N. de Rooij, "Fabrication process of high aspect ratio elastic structures for piezoelectric motor applications", *Sensors and Actuators A: Physical*, vol. 70, no. 2, pp 42-47, 1 October 1998.

## Appendix A: imgFIX Source Code

```
#include <cstdlib>
#include <iostream>
#include <sstream>
#include <sys/types.h>
#include <dirent.h>
#include <errno.h>
#include <vector>
#include <string>
#include <sys/stat.h>
#include <time.h>
#include <unistd.h>
#include <fstream>
#include "convert.h"

using namespace std;

/*function... might want it in some class?*/
int getdir (string dir, vector<string> &files)
{
    DIR *dp;
    struct dirent *dirp;
    if((dp = opendir(dir.c_str())) == NULL) {
        cout << "Error(" << errno << ") opening " << dir << endl;
        return errno;
    }

    while ((dirp = readdir(dp)) != NULL) {
        files.push_back(string(dirp->d_name));
    }
    closedir(dp);
    return 0;
}

std::string getExtension(const std::string& fileName)
{
    const int length = fileName.length();
    for (int i=0; i!=length; ++i)
    {
        if (fileName[i]=='.')
        {
            return fileName.substr(i+1,length);
        }
    }
    return fileName;
}

int main(int argc, char *argv[])
{
    int counter = 0;
    struct tm* clock; // create a time structure
    struct stat attrib; // create a file attribute structure

    int xhour, xmin, xsec, xmon, timestamp;

    int nextday_flag;
    int xmday;

    int houradjust;

    int freq, starttime, stoptime;

    string dir = string(".");
    vector<string> files = vector<string>();
```

```

string logname = "sweep.log";

////////////////////////////////////

cout << "%%%%%%%%%%%%%%%%%%%%%%%%%" << endl;
cout << "%" << endl;
cout << "% Image Renamer - version 0.5" << endl;
cout << "%" << endl;
cout << "% Calin Plesa ( cplesa [at] sfu.ca )" << endl;
cout << "%" << endl;
cout << "% August 22, 2007" << endl;
cout << "%" << endl;
cout << "% Usage:" << endl;
cout << "% imgFIX name-of-sweep-log.file" << endl;
cout << "%" << endl;
cout << "% Warning" << endl;
cout << "% Do not use at midnight (timestamp overflow)" << endl;
cout << "%" << endl;
cout << "%%%%%%%%%%%%%%%%%%%%%%%%%" << endl;
cout << "" << endl;

if (argc > 1) // if log filename given use it
{
    logname = argv[1];
}

cout << "Scanning for .tif files and parsing using " << logname << " :" << endl;
cout << "" << endl;

ifstream in(logname.c_str(), ios::in | ios::binary); //open log file

if(!in) {
    cout << "Cannot open input file.\n";
    return 1;
}
system("mkdir sweep_images");

int frequencylog;

string t;

int currentLine = 1;
int starthour = 0;
int startmin = 0;
int startsec = 0;
int endhour = 0;
int endmin = 0;
int endsec = 0;
char endoffline;

getdir(dir,files);
getline(in, t);
while (!in.eof()) // do for each frequency in the log
{
    std::istringstream i(t.substr(0, 5));
    i >> frequencylog;

    if (frequencylog <= 9999)
    {
        std::istringstream j(t.substr(5, 2));
        j >> starthour;
        std::istringstream k(t.substr(8, 2));
        k >> startmin;
        std::istringstream l(t.substr(11, 2));
        l >> startsec;
    }
}

```

```

        std::istringstream m(t.substr(14, 2));
        m >> endhour;
        std::istringstream n(t.substr(17, 2));
        n >> endmin;
        std::istringstream o(t.substr(20, 2));
        o >> endsec;
    }
    else if (frequencylog > 9999)
    {
        std::istringstream j(t.substr(6, 2));
        j >> starthour;
        std::istringstream k(t.substr(9, 2));
        k >> startmin;
        std::istringstream l(t.substr(12, 2));
        l >> startsec;

        std::istringstream m(t.substr(15, 2));
        m >> endhour;
        std::istringstream n(t.substr(18, 2));
        n >> endmin;
        std::istringstream o(t.substr(21, 2));
        o >> endsec;
    }

    //cout << starthour << " " << startmin << " " << startsec << endl;
    //cout << endhour << " " << endmin << " " << endsec << endl;

    starttime = starthour*3600 + startmin*60 + startsec;
    stoptime = endhour*3600 + endmin*60 + endsec;

    cout << "Frequency: " << frequencylog << " Start Time: " << starttime << " Stop
Time: " << stoptime << endl;

    for (unsigned int i = 0; i < files.size(); i++) { //do for each image
        if (getExtension(files[i]) == "tiff")
        {
            stat(files[i].c_str(), &attrib);
            clock = gmtime(&(attrib.st_mtime));
            xhour = clock->tm_hour;
            xmin = clock->tm_min;
            xsec = clock->tm_sec;
            xmon = clock->tm_mon + 1;

            nextday_flag = 0;
            xmday = 0;

            //////////////////////////////////////
            houradjust = 7; // 7 for Pacific, 4 for Eastern
            //////////////////////////////////////

            if (xhour <= 23 && xhour >= houradjust) // fix hour
            {
                xhour = xhour - houradjust;
            }
            else if (xhour <= (houradjust - 1) && xhour >= 0)
            {
                xhour = xhour + (24 - houradjust);
                nextday_flag = 1;
            }

            if (nextday_flag == 1) // fix day
            {
                xmday = int(clock->tm_mday) - 1;
                nextday_flag = 0;
            }
            else
            {
                xmday = int(clock->tm_mday);
            }
        }
    }

```

```

        timestamp = xhour * 3600 + xmin * 60 + xsec; //xmday * 86400

        //cout << "Frequency: " << frequencylog << " File: " << files[i].c_str()
<< " Time: " << xhour << " " << xmin << " " << xsec << " " << timestamp << endl;

        //cout << timestamp << endl;
        if (timestamp >= starttime && timestamp < stoptime)
        { // if image was created during sweep catch it here
            ostringstream sss;
            cout << "Found: " << files[i] << " " << timestamp << endl;
            sss << "copy " << files[i] << " sweep_images\\" <<

frequencylog << ".tif" ;

            cout << sss.str() << endl;
            system(sss.str().c_str());
            counter++;

        }
    }

    currentLine++;
    cout << "" << endl;
    getline(in, t);
}
in.close();

cout << "Found " << counter << " files in total." << endl;
cout << "" << endl;

system("PAUSE");
return EXIT_SUCCESS;
}

```



## Appendix B: Ideal Resonance Frequencies

**Table 17 - The ideal resonance frequencies of the high aspect Short Beams.**

Length ( $\mu\text{m}$ )	Resonance Frequency (Hz)			
	Width = 10 $\mu\text{m}$		Width = 15 $\mu\text{m}$	
	E = 3.5GPa	E = 4GPa	E = 3.5GPa	E = 4GPa
200	69049	73816	103573	110724
300	30688	32807	46032	49211
400	17262	18454	25893	27681
500	11048	11811	16572	17716
600	7672	8202	11508	12303
700	5637	6026	8455	9039
800	4316	4614	6473	6920
900	3410	3645	5115	5468
1000	2762	2953	4143	4429

**Table 18 - The frequencies of the first two modes for the low aspect ratio Long Beams.**

Length ( $\mu\text{m}$ )	Resonance Frequency (Hz)			
	Width = 75 $\mu\text{m}$			
	1 <sup>st</sup> Mode		2 <sup>nd</sup> Mode	
	E = 3.5GPa	E = 4GPa	E = 3.5GPa	E = 4GPa
200	517865	553621	3241660	3465481
400	129466	138405	810415	866370
600	57541	61513	360184	385053
800	32367	34601	202604	216593
1000	20715	22145	129666	138619
1200	14385	15378	90046	96263
1400	10569	11298	66156	70724
1600	8092	8650	50651	54148
1800	6393	6835	40020	42784
2000	5179	5536	32417	34655
2200	4280	4575	26791	28640
2400	3596	3845	22512	24066
2600	3064	3276	19181	20506
2800	2642	2825	16539	17681
3000	2302	2461	14407	15402
3200	2023	2163	12663	13537